Title
Directionality of dynein is controlled by the angle and length of its stalk

Journal
Nature, 566(7744)

ISSN
0028-0836

Authors
Can, Sinan
Lacey, Samuel
Gur, Mert
et al.

Publication Date
2019-02-01

DOI
10.1038/s41586-019-0914-z

Peer reviewed

LETTER

https://doi.org/10.1038/s41586-019-0914-z

Directionality of dynein is controlled by the angle and length of its stalk

Sinan Can[1,5], Samuel Lacey[2,5], Mert Gur[3], Andrew P. Carter[2] & Ahmet Yildiz[1,4]*

The ability of cytoskeletal motors to move unidirectionally along filamentous tracks is central to their role in cargo transport, motility and cell division. Kinesin and myosin motor families have a subclass that moves towards the opposite end of the microtubule or actin filament with respect to the rest of the motor family[1,2], whereas all dynein motors that have been studied so far exclusively move towards the minus end of the microtubule[3]. Guided by cryo-electron microscopy and molecular dynamics simulations, we sought to understand the mechanism that underpins the directionality of dynein by engineering a *Saccharomyces cerevisiae* dynein that is directed towards the plus end of the microtubule. Here, using single-molecule assays, we show that elongation or shortening of the coiled-coil stalk that connects the motor to the microtubule controls the helical directionality of dynein around microtubules. By changing the length and angle of the stalk, we successfully reversed the motility towards the plus end of the microtubule. These modifications act by altering the direction in which the dynein linker swings relative to the microtubule, rather than by reversing the asymmetric unbinding of the motor from the microtubule. Because the length and angle of the dynein stalk are fully conserved among species, our findings provide an explanation for why all dyneins move towards the minus end of the microtubule.

Dyneins are a family of AAA+ motors that are responsible for nearly all motility, and force generation functions towards the minus end of microtubules[3–5]. Owing to the roles of dynein in intracellular transport, cell division and axonemal beating, defects in dynein motility are linked to many developmental and neurodegenerative disorders[6]. The dynein motor domain contains a catalytic ring of six AAA+ modules (AAA1–AAA6) connected to a microtubule-binding domain (MTBD) by an antiparallel coiled-coil stalk[7] (Fig. 1a). Motility is powered by conformational changes of a linker that resides on the face of the ring. ATP binding to AAA1 triggers microtubule release and moves the linker into a bent conformation; this movement is referred to as the priming stroke[3]. After ATP hydrolysis, dynein rebinds to the microtubule and the linker returns to its straight conformation[8–11], which serves as the force-generating power stroke of dynein[11] (Extended Data Fig. 1).

There are two current models of the mechanism that underlies dynein directionality. The linker swing vector (LSV) model suggests that the motor domain pivots around the linker, and that its stepping follows the direction in which the linker swings relative to the microtubule[8,12,13] (Extended Data Fig. 1). Because dynein has multiple flexible elements in its structure[14,15], it remains unclear whether the LSV mechanism is capable of providing a net bias towards the minus end during stepping. Alternatively, the asymmetric release model proposes that the faster release of dynein when it is pulled towards the minus end[5,16,17] creates a net bias in minus-end directionality. Consistent with this model, an engineering study[18] that replaced the MTBD of dynein with actin-binding proteins suggested that unidirectional motility can be facilitated by asymmetric release from the cytoskeletal track, regardless of the direction in which the LSV is pointed.

We tested the LSV model by altering the direction in which the linker swings and determining how this affects dynein motility. According to the LSV model, pointing the LSV sideways, relative to the microtubule, would create a net bias in the helical directionality of dynein around the circumference of microtubules. All-atom molecular dynamics simulations predicted that elongating or shortening the coiled-coils of the stalk by three heptads (to produce Dyn_{+3hep} or Dyn_{-3hep}, respectively) would rotate the AAA+ ring around the stalk axis and shift the LSV rightward or leftward, respectively, along the short axis of the microtubule (the LSV_{short}; Fig. 1a, b, Extended Data Figs. 2, 3). We determined the helical directionality of dynein-driven beads on microtubule bridges[19]. As previously observed[20,21], the beads driven by native dynein (Dyn) monomers moved in both clockwise and anticlockwise helical trajectories without a significant sideways bias ($P = 0.05$, Student's *t*-test; Fig. 1c, d). By contrast, beads driven by Dyn_{+3hep} monomers rotated mostly clockwise, and Dyn_{-3hep} rotated the beads anticlockwise around microtubules (Fig. 1c, d, Supplementary Video 1), consistent with the predicted directions of their LSV_{short} (Fig. 1a, b, Extended Data Fig. 3). We concluded that the stalk length of native dynein is critical for restricting sideways movement and for directing motility primarily along the long axis of the microtubule.

Altering the stalk length, which rotates the AAA+ ring relative to the stalk axis, did not affect the minus-end directionality of dynein motility[12] (Extended Data Fig. 3d). This could be because the stalk of dynein is tilted about 45° towards the plus end (Fig. 2a), which points the LSV long-axis component (the LSV_{long}) to the minus end[12,14,22] (Fig. 2d). To change the stalk angle, we shifted the positions of two fully conserved proline residues at the base of the MTBD along the coiled-coils of the stalk (Extended Data Figs. 2, 4, 5). Molecular dynamics simulations indicated that a dynein mutant with a two-residue shift of both prolines ('reverse kink', labelled Dyn_{RK}; Extended Data Fig. 2) can fold properly into a well-ordered structure in which the stalk is tilted in the reverse direction of Dyn (Fig. 2b, c, Extended Data Fig. 6, Supplementary Video 2). Simulations also predicted that pointing the LSV_{long} towards the plus end requires not only the tilting of stalk towards the minus end, but also a reversal of the ring relative to the stalk axis with an elongation of seven heptads ($Dyn_{RK+7hep}$, Fig. 2b–d, Extended Data Fig. 2).

To test the structural predictions of the molecular dynamics simulations, we used cryo-electron microscopy (cryo-EM) to image Dyn and $Dyn_{RK+7hep}$ monomers bound to microtubules (Extended Data Fig. 7). Two-dimensional classification of $Dyn_{RK+7hep}$ showed that the stalk length was extended to 18.5 ± 1.9 nm (compared to 12.7 ± 1.2 nm for Dyn (Fig. 2e, mean ± s.d.)), which is compatible with the predicted 7-nm elongation of the stalk owing to the 7-heptad insertion (Extended Data Fig. 6). Centred on a pivot at the base of the stalk, a broad range of stalk angles was observed for both Dyn and $Dyn_{RK+7hep}$ (Fig. 2f, Supplementary Video 3). The average stalk angle of Dyn was measured as 55 ± 26° (refs [12,14,22]) (Fig. 2f). $Dyn_{RK+7hep}$ had a wider distribution of stalk angles, and the majority of the molecules had their stalk tilted in the opposite direction to that of Dyn (111 ± 35°, mean ± s.d.). Density for the linker remains below the ring for $Dyn_{RK+7hep}$ (Fig. 2e), which

[1]Physics Department, University of California at Berkeley, Berkeley, CA, USA. [2]Medical Research Council, Laboratory of Molecular Biology, Division of Structural Studies, Cambridge, UK. [3]Department of Mechanical Engineering, Istanbul Technical University, Istanbul, Turkey. [4]Department of Molecular and Cellular Biology, University of California at Berkeley, Berkeley, CA, USA. [5]These authors contributed equally: Sinan Can, Samuel Lacey. *e-mail: yildiz@berkeley.edu

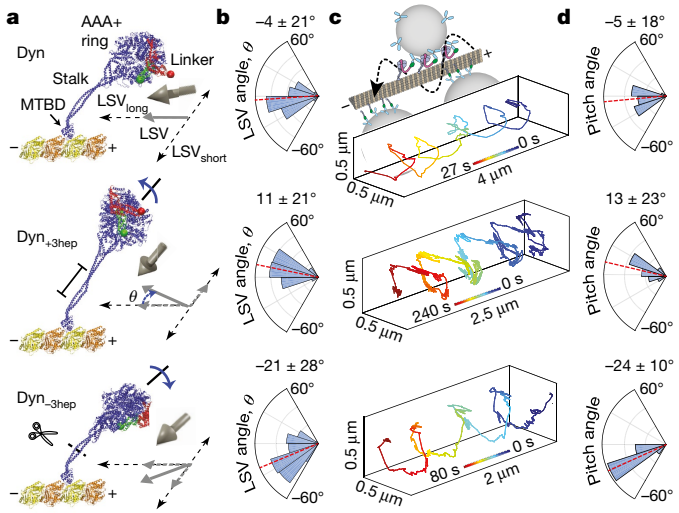

Fig. 1 | The stalk length is critical to align dynein motility along the long axis of the microtubule. a, A dynein head is superimposed onto a microtubule and the linker is highlighted in its pre- (red) and post-power stroke (green) conformation (RCSB Protein Data Bank (PDB) accession numbers: 3VKG, 4RH7 and 3J1T). The LSV (grey arrow) is defined as the displacement of the linker from the pre- (red bead) to post-powerstroke (green bead) conformation. The projection of the LSV to the long axis of the microtubule is pointed towards the minus end for Dyn (see Methods). Dyn$_{+3hep}$ and Dyn$_{-3hep}$ were modelled by a three-heptad insertion or deletion of the stalk, respectively, and re-alignment of the stalk coiled-coils in Dyn conformations (obtained from molecular dynamics simulations). Changing the stalk length is expected to rotate the ring and project the LSV sideways (by angle θ). **b**, Calculated LSV angles from molecular dynamics simulations (mean ± s.d., $n = 1{,}680$ conformations from 3 different simulations). **c**, Top, Schematic of helical motility of 0.5-μm diameter cargo beads driven by monomeric dyneins around a microtubule bridge. Bottom, example trajectories of beads driven by Dyn, Dyn$_{+3hep}$ and Dyn$_{-3hep}$. Cargo beads carried by Dyn$_{+3hep}$ and Dyn$_{-3hep}$ rotate clockwise and anticlockwise, respectively, around the microtubule. **d**, Histograms of the pitch angles (mean ± s.d.; from top to bottom, $n_{beads} = 24$, 20 and 19 and $n_{rotations} = 99$, 59 and 72, from 2 independent experiments).

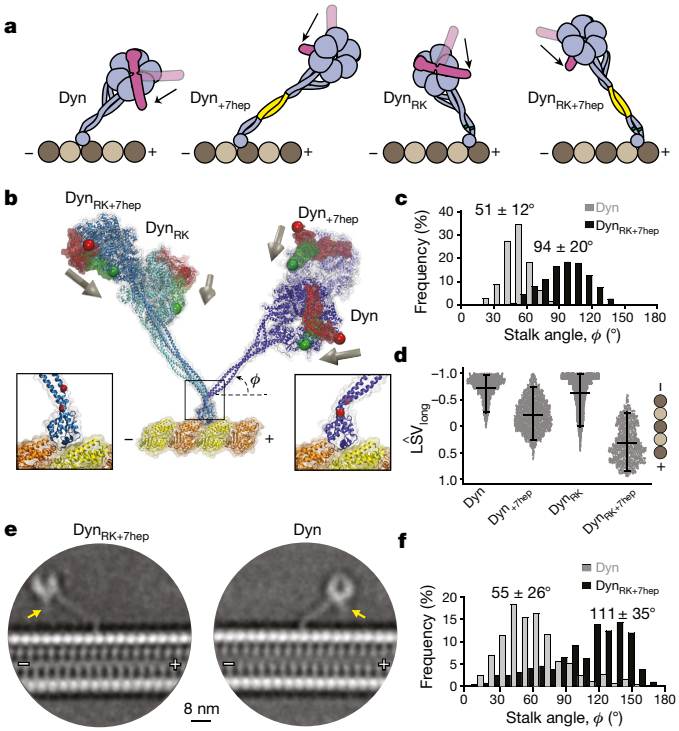

Fig. 2 | The stalk angle is reversed by shifting the position of two conserved prolines. a, Expected LSV$_{long}$ orientation (black arrow) in Dyn, Dyn$_{+7hep}$, Dyn$_{RK}$ and Dyn$_{RK+7hep}$. Altering both the angle and length of the stalk in Dyn$_{RK+7hep}$ is expected to direct the LSV$_{long}$ towards the plus end of the microtubule. **b**, Example snapshots from all-atom molecular dynamics simulations for tail-truncated dynein monomers in the pre-power stroke conformation docked onto a microtubule. The post-power stroke conformation of the linker was superimposed to calculate the LSV orientation (grey arrows). Right insert, simulations confirmed the plus-end-directed tilt of the Dyn stalk, owing to two conserved proline residues (red) at its base. Left insert, Dyn$_{RK}$ and Dyn$_{RK+7hep}$ can fold into a reverse kink structure by shifting the positions of the proline residues two positions away from the MTBD. **c**, Stalk angle (ϕ) distributions from Dyn and Dyn$_{RK+7hep}$ simulations ($n = 1{,}680$ and 2,270 conformations for Dyn and Dyn$_{RK+7hep}$, respectively; mean ± s.d., $P = 10^{-59}$). **d**, The length of the LSV unit vector ($\hat{LSV}_{long}$) projected onto the long axis of the microtubule, measured by molecular dynamics simulations (mean ± s.d.). −1 corresponds to LSV pointed towards the minus end. The centre line and edges represent the mean and 5–95% confidence intervals, respectively ($n = 1{,}680$, 1,680, 11,637 and 2,270 from left to right; $P = 10^{-59}$, 10^{-55} or 10^{-59} for Dyn versus Dyn$_{+7hep}$, Dyn$_{RK}$ or Dyn$_{RK+7hep}$, respectively). **e**, Cryo-EM 2D class averages of Dyn and Dyn$_{RK+7hep}$ monomers bound to a microtubule show different orientations of their stalk. Arrows point to the N terminus of the linker. **f**, The histogram of the stalk angles for Dyn ($n = 392$) and Dyn$_{RK+7hep}$ ($n = 421$), relative to the long axis of the microtubule (mean ± s.d., $P = 10^{-15}$). 180° represents the tilting of the stalk towards the minus end of the microtubule. *P* values are calculated using a two-sided *t*-test.

shows that the ring is rotated relative to its stalk axis. These results confirm that our modifications reverse the stalk angle and rotate the ring relative to the stalk axis.

We next tested whether mutations of the Dyn$_{RK+7hep}$ stalk disrupt the mechanical properties that are crucial for robust dynein motility[23,24]. The affinity of monomeric Dyn$_{RK+7hep}$ for microtubules was similar to Dyn under different nucleotide conditions (Fig. 3a). Dyn$_{RK+7hep}$ showed robust microtubule-stimulated ATPase activity, albeit with an elevated basal ATPase rate and slightly lower catalytic rate, compared to Dyn (Fig. 3b, Extended Data Table 1a). We also determined how external load affects the velocity and microtubule release of Dyn$_{RK+7hep}$ using an optical trap. Similar to Dyn[25], full-length Dyn$_{RK+7hep}$ moved processively towards the direction of applied load in the absence of nucleotide. Velocity increased continuously when the motor was pulled towards the minus end, whereas the motility was slow when pulled towards the plus end (Fig. 3c, d). The rates of force-induced microtubule release of the Dyn$_{RK+7hep}$ monomer are similar to those to Dyn, rapidly releasing from microtubules when pulled towards the minus end and resisting a plus-end-directed pull of the optical trap (Fig. 3e, f, Extended Data Fig. 8). Therefore, the mutations that we introduced into Dyn$_{RK+7hep}$ do not disrupt nucleotide-dependent communication between the ring and MTBD, or the asymmetric release from the microtubule.

We inserted these mutations into tail-truncated, GST-dimerized dynein[4] and tested the directionality of their motility in microtubule gliding assays (Fig. 4a). Dyn$_{RK}$ motors exhibited very slow motility towards the minus end (Fig. 4b, Supplementary Video 4), which is consistent with the predicted direction of the LSV of Dyn$_{RK}$ (Fig. 2d). By contrast, Dyn$_{RK+7hep}$ glided all microtubules towards the plus end (Fig. 4b), which demonstrates that modifications in this construct successfully reverse dynein directionality. Increasing the ionic strength resulted in a faster gliding velocity of both Dyn and Dyn$_{RK+7hep}$, without affecting their directionality (Fig. 4b, Supplementary Video 5). We also observed robust plus-end directionality of multiple monomeric Dyn$_{RK+7hep}$ motors in microtubule gliding and bead-motility assays (Extended Data Fig. 9, Supplementary Video 7).

In single-molecule motility assays (Fig. 4c), 90% of full-length Dyn$_{RK+7hep}$ dimers walked processively by taking steps towards the plus end (Fig. 4d, e, Extended Data Table 1a, Supplementary Video 6). The average step size of Dyn$_{RK+7hep}$ in the plus-end direction was slightly higher (14.1 ± 7.7 nm) than the step size of Dyn towards the minus end (13.0 ± 6.7 nm; $P = 0.026$, *t*-test), which suggests that lengthening

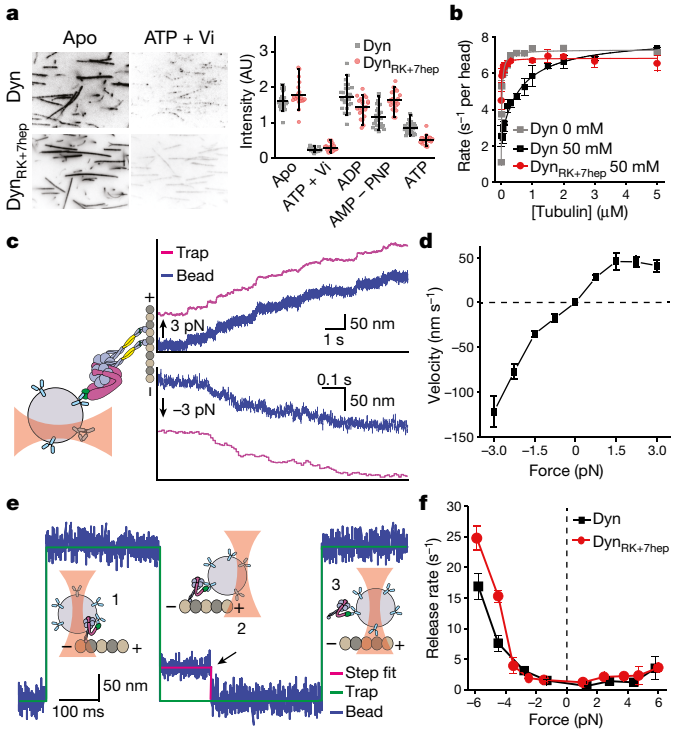

Fig. 3 | Reversal of the stalk angle does not disrupt nucleotide- and force-induced release of dynein from the microtubule. a, Representative images (left), and the intensity of 100 nM GFP-tagged Dyn and Dyn$_{RK+7hep}$ monomers on sea urchin axonemes under given nucleotide conditions (right). Similar to Dyn, Dyn$_{RK+7hep}$ released from microtubules in the ADP-P$_i$ state, mimicked by ATP and vanadate (Vi, $n = 40$ axonemes from three independent measurements, mean ± 95% confidence intervals). **b**, Microtubule-stimulated ATPase activity of dynein in 2 mM ATP (mean ± s.d. from three independent measurements) under different salt concentrations. Solid curves represent fit to the Michaelis–Menten kinetics. **c**, Left, full-length Dyn$_{RK+7hep}$ was attached to a polystyrene bead and pulled by constant load using an optical trap (not to scale). Right, representative trajectories of single Dyn$_{RK+7hep}$ when pulled by 3 pN towards the plus end (positive forces, $n = 20$ beads) or minus end (negative forces, $n = 20$ beads) of a microtubule. **d**, Force–velocity relationship of Dyn$_{RK+7hep}$ in the apo condition (mean ± s.e.m., $n = 20$, 21, 19, 16, 15, 23, 15, 15 and 20 beads, from left to right). **e**, Dynein monomers were attached to a polystyrene bead through their linker and oscillated ± 150 nm along the long axis of the microtubule by optical trap (1). When a molecule binds to the microtubule (2), the movement of the bead to the next trap position is restricted and the trap exerts a constant force until the motor releases from the microtubule (the black arrow) and the bead follows the trap (3). **f**, Similar to Dyn, Dyn$_{RK+7hep}$ favours faster release from a microtubule when pulled towards the minus end. Rates are calculated from an exponential decay fit to the dwell-time histograms ($n = 120$ dwells for each force range, from two biological replicates; mean ± s.d.).

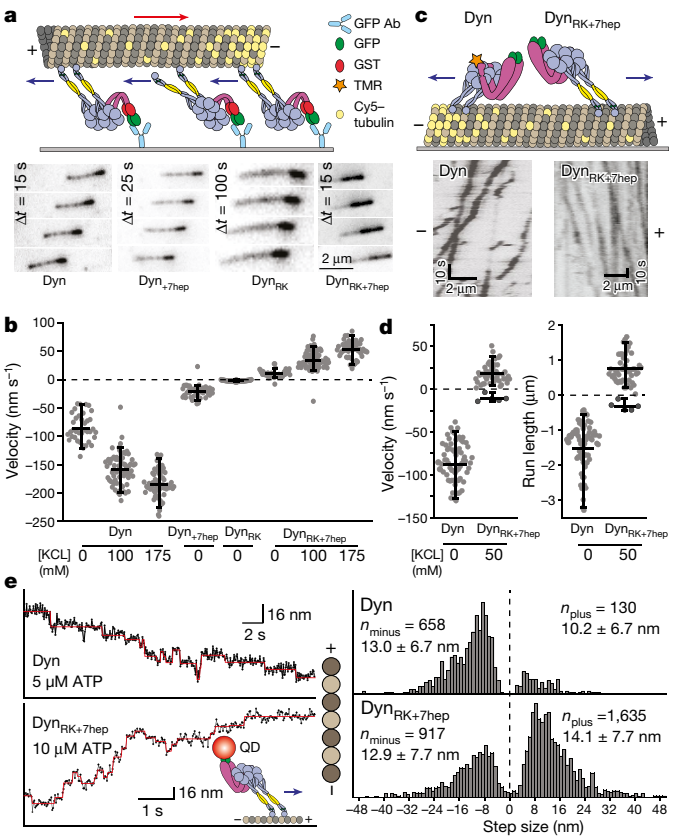

Fig. 4 | The directionality of dynein is reversed by altering the length and the angle of its stalk. a, Top, schematic of microtubule gliding activity of surface-immobilized dyneins. Bottom, time-lapse recordings show that Dyn, Dyn$_{+7hep}$ and Dyn$_{RK}$ glide microtubules with the plus end ahead, whereas Dyn$_{RK+7hep}$ glides microtubules towards the opposite direction. **b**, Microtubule gliding velocity and directionality of dynein mutants at given salt concentrations. Negative velocities correspond to minus-end-directed motility. $n = 38$, 69, 60, 49, 59, 49, 83 and 53 microtubules, from left to right ($P = 10^{-46}$ or 10^{-43} for Dyn versus Dyn$_{RK}$ or Dyn$_{RK+7hep}$, respectively). **c**, Top, schematic of single-molecule motility assays. Bottom, example kymographs show processive motility of Dyn and Dyn$_{RK+7hep}$ dimers. **d**, Velocity and run length of Dyn and Dyn$_{RK+7hep}$ dimers. $n = 67$ (Dyn) and 52 (Dyn$_{RK+7hep}$) motors ($P = 10^{-45}$). **e**, Left, example trajectories of quantum-dot (QD)-labelled Dyn and Dyn$_{RK+7hep}$ stepping along microtubules. The position of the quantum dot (solid dots) was fit by a step-finding algorithm (red lines). Right, histogram of step-size distribution (mean ± s.d.). In **b** and **d**, the centre line and edges represent the mean and 5–95% confidence intervals, respectively. In **d** and **e**, mean values for plus- and minus-end-directed runs and steps are calculated separately. *P* values are calculated using a two-sided *t*-test.

the stalk causes a modest increase in step size. When we compared backward-stepping, Dyn$_{RK+7hep}$ took minus-end-directed steps more frequently than Dyn took plus-end-directed steps (35% versus 16%, χ^2 test, $P = 10^{-24}$; Fig. 4e). This might result from tension-induced stepping, which favours minus-end-directed stepping of both Dyn[16,17,20,21] and Dyn$_{RK+7hep}$ (Fig. 3c–f). Collectively, these results provide direct evidence that dynein directionality is reversed when the LSV is pointed towards the plus end. Because Dyn$_{RK+7hep}$ and Dyn share the same response to applied tension, but move in opposite directions, our results are inconsistent with tension-induced release as the primary mechanism of dynein directionality.

In this study, we successfully directed dynein motility leftward, rightward and backward by altering the direction of LSV. Two critical features of the dynein stalk—the length of its antiparallel coiled-coils and the sharp angle it makes relative to the microtubule—direct LSV towards the minus end of the microtubule. Both of these features are fully conserved in cytoplasmic and ciliary dyneins across species[26] (Extended Data Figs. 4, 5), which suggests that all dyneins are minus-end-directed motors. Inner-arm dyneins typically have additional proline residues in their stalk, which may alter the LSV for generating ciliary waveforms.

Our study also provides fresh insights into how dynein provides a net bias for unidirectional motility during its mechanochemical cycle. Because dynein heads step independent of each other[20,21], a single head of a dynein dimer must be able to release from the microtubule, move forward and rebind the microtubule without a need for pulling or pushing of its partner head[16,20]. We propose that as the stepping head releases from the microtubule, the priming stroke of its linker biases the stepping direction towards the minus end. After the head rebinds to the microtubule, the power stroke of its linker pulls the cargo towards the minus end[8,13] (Extended Data Fig. 1). This tethered excursion mechanism is fundamentally distinct from the directionality of kinesin-1 and

myosin-V, in which the power stroke of the head in the leading position pulls the lagging head forward[1,2].

Online content

Any methods, additional references, Nature Research reporting summaries, source data, statements of data availability and associated accession codes are available at https://doi.org/10.1038/s41586-019-0914-z.

Received: 13 February 2018; Accepted: 9 January 2019;
Published online 6 February 2019.

1. Bryant, Z., Altman, D. & Spudich, J. A. The power stroke of myosin VI and the basis of reverse directionality. *Proc. Natl Acad. Sci. USA* **104**, 772–777 (2007).
2. Sablin, E. P. et al. Direction determination in the minus-end-directed kinesin motor ncd. *Nature* **395**, 813–816 (1998).
3. Roberts, A. J., Kon, T., Knight, P. J., Sutoh, K. & Burgess, S. A. Functions and mechanics of dynein motor proteins. *Nat. Rev. Mol. Cell Biol.* **14**, 713–726 (2013).
4. Reck-Peterson, S. L. et al. Single-molecule analysis of dynein processivity and stepping behavior. *Cell* **126**, 335–348 (2006).
5. Gennerich, A., Carter, A. P., Reck-Peterson, S. L. & Vale, R. D. Force-induced bidirectional stepping of cytoplasmic dynein. *Cell* **131**, 952–965 (2007).
6. King, S. M. (ed.) *Dyneins, Dynein Mechanics, Dysfunction and Disease* Vol. 2, 2nd edn (Academic, London, 2017).
7. Gee, M. A., Heuser, J. E. & Vallee, R. B. An extended microtubule-binding structure within the dynein motor domain. *Nature* **390**, 636–639 (1997).
8. Roberts, A. J. et al. AAA+ ring and linker swing mechanism in the dynein motor. *Cell* **136**, 485–495 (2009).
9. Schmidt, H., Gleave, E.S. & Carter, A.P. Insights into dynein motor domain function from a 3.3-Å crystal structure. *Nat. Struct. Mol. Biol.* **19**, 492–497 (2012).
10. Kon, T. et al. The 2.8 Å crystal structure of the dynein motor domain. *Nature* **484**, 345–350 (2012).
11. Schmidt, H., Zalyte, R., Urnavicius, L. & Carter, A. P. Structure of human cytoplasmic dynein-2 primed for its power stroke. *Nature* **518**, 435–438 (2015).
12. Carter, A. P. et al. Structure and functional role of dynein's microtubule-binding domain. *Science* **322**, 1691–1695 (2008).
13. Lin, J., Okada, K., Raytchev, M., Smith, M. C. & Nicastro, D. Structural mechanism of the dynein power stroke. *Nat. Cell Biol.* **16**, 479–485 (2014).
14. Imai, H. et al. Direct observation shows superposition and large scale flexibility within cytoplasmic dynein motors moving along microtubules. *Nat. Commun.* **6**, 8179 (2015).
15. Lippert, L. G. et al. Angular measurements of the dynein ring reveal a stepping mechanism dependent on a flexible stalk. *Proc. Natl Acad. Sci. USA* **114**, E4564–E4573 (2017).
16. Cleary, F. B. et al. Tension on the linker gates the ATP-dependent release of dynein from microtubules. *Nat. Commun.* **5**, 4587 (2014).
17. Nicholas, M. P. et al. Cytoplasmic dynein regulates its attachment to microtubules via nucleotide state-switched mechanosensing at multiple AAA domains. *Proc. Natl Acad. Sci. USA* **112**, 6371–6376 (2015).
18. Furuta, A. et al. Creating biomolecular motors based on dynein and actin-binding proteins. *Nat. Nanotechnol.* **12**, 233–237 (2017).
19. Can, S., Dewitt, M. A. & Yildiz, A. Bidirectional helical motility of cytoplasmic dynein around microtubules. *eLife* **3**, e03205 (2014).
20. DeWitt, M. A., Chang, A. Y., Combs, P. A. & Yildiz, A. Cytoplasmic dynein moves through uncoordinated stepping of the AAA+ ring domains. *Science* **335**, 221–225 (2012).
21. Qiu, W. et al. Dynein achieves processive motion using both stochastic and coordinated stepping. *Nat. Struct. Mol. Biol.* **19**, 193–200 (2012).
22. Redwine, W. B. et al. Structural basis for microtubule binding and release by dynein. *Science* **337**, 1532–1536 (2012).
23. Gibbons, I. R. et al. The affinity of the dynein microtubule-binding domain is modulated by the conformation of its coiled-coil stalk. *J. Biol. Chem.* **280**, 23960–23965 (2005).
24. Kon, T. et al. Helix sliding in the stalk coiled coil of dynein couples ATPase and microtubule binding. *Nat. Struct. Mol. Biol.* **16**, 325–333 (2009).
25. Belyy, V., Hendel, N. L., Chien, A. & Yildiz, A. Cytoplasmic dynein transports cargos via load-sharing between the heads. *Nat. Commun.* **5**, 5544 (2014).
26. Niekamp, S., Coudray, N., Zhang, N., Vale, R. D. & Bhabha, G. Stalk-mediated communication in the dynein motor domain. Preprint at https://www.biorxiv.org/content/early/2018/04/27/309179 (2018).

Acknowledgements We thank F. B. Cleary, H. Schmidt, C. Cypranowska, V. Belyy and L. Ferro for initiation of this project; S. Chen, C. Savva, G. Cannone, J. Grimmett, T. Darling and L. Kellogg for technical assistance with cryo-EM; M. Mofrad and M. Mehrbod for coarse-grained simulations; and the Savio Cluster for molecular dynamics simulations. This work was funded by grants from the NIH (GM094522), and NSF (MCB-1055017, MCB-1617028) to A.Y., the Wellcome Trust (WT100387) and the Medical Research Council, UK (MC_UP_A025_1011) to A.P.C., and TUBITAK (215Z398) and ITU BAP (38777) to M.G.

Reviewer information *Nature* thanks W. Hancock and the other anonymous reviewer(s) for their contribution to the peer review of this work.

Author contributions A.Y. and A.P.C. initiated the project. S.C. engineered dynein mutants and performed motility assays. S.L. performed cryo-EM imaging. M.G. performed molecular dynamics simulations. A.Y., S.C., A.P.C. and M.G. prepared the manuscript. A.Y., A.P.C. and M.G. supervised the project.

Competing interests The authors declare no competing interests.

Additional information
Extended data is available for this paper at https://doi.org/10.1038/s41586-019-0914-z.
Supplementary information is available for this paper at https://doi.org/10.1038/s41586-019-0914-z.
Reprints and permissions information is available at http://www.nature.com/reprints.
Correspondence and requests for materials should be addressed to A.Y.
Publisher's note: Springer Nature remains neutral with regard to jurisdictional claims in published maps and institutional affiliations.

METHODS

No statistical methods were used to predetermine sample size. The experiments were not randomized and investigators were not blinded to allocation during experiments and outcome assessment.

Construct design, protein expression and labelling. An N-terminally truncated *S. cerevisiae* cytoplasmic dynein gene (*DYN1*) encoding amino acids 1219–4093 (predicted molecular mass 331 kDa; referred to as Dyn) was used as a template for mutagenesis. Constructs were prepared by gene synthesis of the stalk region. DNA fragments were inserted into the genome of haploid yeast cells by homologous recombination to replace a URA3 cassette (Extended Data Fig. 2). *S. cerevisiae* strains were received from R. Vale (UCSF) and were not authenticated or tested for mycoplasma contamination. A ZZ affinity tag and a TEV protease cleavage site were inserted into the N terminus for purification and a DHA tag was inserted at the N- or C termini for labelling[4] (Extended Data Table 1b). The constructs were purified by binding the cell lysate to IgG beads and cleaving the protein from the beads with Tev protease[4]. Motors were labelled with 10 μM fluorescent dyes functionalized with alkyl chloride when bound to IgG beads, and the excess dye was removed before Tev cleavage.

Electron microscopy sample preparation. Lyophilized porcine brain tubulin (cytoskeleton) was resuspended to 10 mg ml^{-1} in MES-MT buffer (30 mM MES pH 6.5, 70 mM NaCl, 1 mM $MgCl_2$, 1 mM DTT) and aliquoted. For polymerization, aliquots were diluted twofold in MES-MT buffer supplemented with 6 mM GTP (Sigma), followed by incubation at 37 °C for 90 min. A further twofold dilution in MES-MT buffer supplemented with 20 μM taxol was made, and the microtubules were left at room temperature overnight. Monomeric Dyn or $Dyn_{RK+7hep}$ was diluted fivefold into cold BRB10 (10 mM PIPES pH7.0, 1 mM EGTA, 1 mM $MgCl_2$, 1 mM DTT, 0.1% Tween-20), and concentrated to the original volume in an Amicon 100 MWCO 0.5-ml centrifugal concentrator. Complete buffer exchange was achieved through two further cycles of dilution and concentration, resulting in a total dilution factor of 125. Microtubules were pelleted at 20,000 r.c.f. for 10 min and resuspended in room temperature BRB10. Three minutes before grid freezing, a mixture containing 1 μM microtubule and 150 nM dynein was made up in room temperature BRB10. Then, 4 μl of this sample was applied to Quantifoil Au300 R1.2/1.3 grids held in a FEI Vitrobot III chamber set to 100% humidity, 22 °C. Following 4–4.5 s blotting, the grid was plunged into liquid ethane and stored in liquid nitrogen until imaging.

Electron microscopy imaging and data analysis. Grids were loaded into a Gatan 626 cryo-holder and imaged in an FEI F20 TEM operating at 200 kV, equipped with a Falcon II detector reading out a single integrated average. Images were semi-automatically acquired with EPU, at a defocus of −4 μm, a flux of 50 e Å^{-2} s^{-1}, an exposure of 1.5 s and a pixel size of 2.06 Å^2. Analysis of dynein on microtubules was performed as previously described[14]. Contrast transfer function was determined using GCTF, and micrographs were phase-flipped accordingly in Relion. Microtubule polarity was determined in FIJI[27] (Extended Data Fig. 5c–g), and the microtubules were boxed out into new images such that their plus end pointed towards the right of the image. The microtubule was duplicated and reflected through the long axis to ensure all unique particles were on the top edge. Monomeric dyneins were picked manually in Relion, and centred at the point at which the stalk reaches the top edge of the microtubule. Particles were disregarded if the kink at the base of the stalk was not observed, or if any neighbouring particles overlapped. Two-dimensional classification into a single class each (for Dyn and $Dyn_{RK+7hep}$) aligned the particles to each other. The angle of the stalk relative to the long axis of the microtubule, and stalk length, was measured for each particle in FIJI.

To simulate projections of the motor on a microtubule the following PDB entries were used: 3VKG[10] (for the stalk) and 4AI6[11] (for the ADP-bound state of the ring and linker). The coordinates were converted into a simulated electron density volume with the EMAN program 'pdb2mrc'. The volume was bandpass filtered between 30 Å and 500 Å using 'bfilter', and projected in different orientations in Relion.

Fluorescence microscopy. Assays were performed on a custom-built objective-type total internal reflection fluorescence (TIRF) microscope, equipped with Nikon Ti-Eclipse inverted microscope body, the perfect focusing system, and a 1.49 NA 100× oil immersion objective (Nikon). The fluorophores were excited with 488 nm (for GFP and QDs) and 561 nm (for TMR and Cy3) and 633 nm (for Cy5) lasers, and the fluorescent signal was detected by the EM-CCD camera (Ixon, Andor) with an effective pixel size of 106 nm. The videos were recorded at 1 Hz. For dual colour imaging, fluorescence emission was separated into two channels on a CCD camera using Optosplit II (Cairn) image splitter.

Microtubule-bridge assays. Bead-motility assays on microtubule bridges were performed as previously described[19]. In brief, 2-μm diameter polystyrene beads were coated with an anti-GFP antibody (Covance) using EDC-NHS crosslinking. The beads were incubated with 0.5 μM $SRS_{85:82}$–GFP[23] and excess protein was removed by pelleting the beads. The beads were non-specifically adsorbed to the surface of the flow chamber and the surface was pre-blocked with 30 μl DLBC (DLB buffer (30 mM HEPES pH 7.4, 1 mM EGTA, 2 mM $MgCl_2$, and 10% glycerol) supplemented with 1 mg ml^{-1} casein). Cy3-labelled microtubules (0.015 mg ml^{-1}) were flown into the chamber. After 10 min, unbound microtubules were removed by a 30-μl DLBC wash. Anti-GFP antibody-coated beads (0.5-μm diameter) were incubated on ice with 5–10 nM GFP–dynein for 10 min and flown into the chamber in the imaging buffer. The sample was placed on a bright-field microscope equipped with a Nikon Ti-E Eclipse microscope body, a Nikon 100× 1.49 NA oil immersion objective, Nikon 1.4 NA oil condenser and LED white-light illuminator (Sutter). The sample was scanned for a microtubule bridge that is longer than 10 μm and oscillates less than 2 pixels. The spontaneous attachment of freely diffusing dynein-coated beads and their processive motility along the microtubule bridges were captured with the CMOS camera (Hamamatsu) at 10 Hz with an effective pixel size of 57 nm. Cargo beads were tracked using a Gaussian fitting algorithm in MATLAB. The helical pitch (λ) was calculated from the periodicity of the x–y projection of the traces between peak-to-peak positions[19]. The distance between the centre of the microtubule cylinder and pivoting point of dyneins at their linker domains (r) was estimated to be 27 nm. The pitch angle was defined as $\tan^{-1}(2\pi r/\lambda)$. The z position of a bead was calibrated by measuring the intensity of surface immobilized 0.5-μm beads while the microscope objective was moved ± 250 nm in the z-direction with 25-nm increments using a piezoelectric objective scanner (Physik Instrumente).

Gliding assays. To polarity-mark the microtubules, *N*-ethylmaleimide (NEM) modified tubulin was prepared by mixing 10 mg ml^{-1} unlabelled tubulin (purified from porcine brain[28]) in BRB80 (80 mM PIPES pH 6.8, 1 mM EGTA, 2 mM $MgCl_2$) with 1 mM NEM and 0.5 mM GTP for 10 min on ice. The reaction is quenched with 8 mM β-mercaptoethanol (βME) for 30 min on ice. Brightly labelled microtubule seeds were polymerized by incubating 0.4 mg ml^{-1} Cy3-labelled tubulin, 0.5 mg ml^{-1} unlabelled tubulin, 1 mM GMP–CPP (Jena BioSciences) and 1 mM DTT in BRB80 for 15 min at 37 °C. The 1.5 μl seed was added to a mixture containing 0.1 mg ml^{-1} Cy3-tubulin, 1 mg ml^{-1} unlabelled tubulin, 1 mg ml^{-1} NEM-modified tubulin, 1 mM GTP and 1 mM DTT in BRB80 and incubated at 37 °C. Immediately after mixing, 2 μl of 2 μM, 20 μM and 200 μM taxol was added with 10 min breaks. After an additional 15-min incubation at 37 °C, microtubules were pelleted over 300 μl 30% glycerol cushion at 65,000g for 10 min. The pellet was resuspended in BRB80 with 20 μM taxol and 1 mM DTT and stored in dark at room temperature. Polarity-marked microtubules were prepared fresh daily for the gliding assays.

For microtubule gliding assays[4], rabbit monoclonal anti-GFP antibody (~0.4 mg ml^{-1}, Covance) was flown to an assay chamber and incubated for 5 min. The chamber was washed with 60 μl of buffer DLBCT (DLBC supplemented with 20 μM taxol). Subsequently, 10 μl of 20 nM GFP-tagged motor in DLBCT was added to the chamber. After a 3-min incubation, unbound motor was removed by 30-μl DLBCT wash. Then, 10 μl of 200 nM freshly polymerized polarity-marked microtubules were flown to the chamber and allowed to bind dynein for 2 min. The chamber was washed with 100 μl of DLBCT. Lastly, 30 μl of imaging buffer (DLBCT supplemented with 2.5 mM PCA (protocatechuic acid), 50 nM PCD (protocatechuate-3,4-dioxygenase) and 1 mM ATP) containing the desired KCl concentration was flown to the chamber.

Single-molecule motility assays. Sea urchin axonemes were immobilized on a glass coverslip in a flow chamber. The chamber was washed with 50 μl DLBC. GFP-tagged mutant dynein (0.2 nM) and TMR-tagged wild-type dynein (0.2 nM) were added into the chamber in DLBC and allowed to bind microtubules for 3 min. The chamber was then washed with 100 μl DLBC and 20 μl imaging buffer. Two fluorescent channels were overlaid, and the velocity and directionality of the constructs was determined with kymograph analysis using ImageJ.

For high-resolution tracking assays, 655 nm amine-labelled QDs (Invitrogen) were coated with anti-GFP antibody by using sulfo-SMCC (sulfosuccinimidyl 4-(*N*-maleimidomethyl) cyclohexane-1-carboxylate) as a cross-linking reagent. QDs (100 nM) were mixed with 25 μM sulfo-SMCC (~250-fold molar excess) and incubated for 1 h. Excess sulfo-SMCC was removed by using 30k MWCO spin-concentrator with 3 consecutive dilutions into DLB. Anti-GFP antibodies (0.4 mg ml^{-1}) were reduced with 4 mM TCEP (tris (2-carboxyethyl) phosphine) for 30 min and mixed with QDs. After 1 h, excess antibody was removed by using spin filter for 3 consecutive dilutions into 25 mM sodium borate buffer pH 8.0, and concentrated to 5 μM for storage. All reactions were performed at room temperature.

Anti-GFP antibody-labelled QDs (5 mM) were mixed with 100 nM GFP-tagged dynein with 1:1 ratio and incubated 15 min on ice. Polarity-marked and biotinylated microtubules were immobilized on the coverslips using biotinylated-BSA and streptavidin. Dynein–QD mixture was diluted 100-fold and was flown into the chamber. After a 3-min incubation, the chamber was washed with 100 μl DLBC and 20 μl imaging buffer containing 5–10 μM ATP. Two fluorescent channels of Cy3-labelled microtubules and QDs were overlaid to determine the directionality

of the motility at 20-ms temporal resolution. Comparison of the number of GFP versus QD spots that moved along microtubules suggested that ~10% of dyneins were labelled with a QD under these conditions.

The QD position was tracked by fluorescence imaging with one-nanometre accuracy (FIONA)[29] using a two-dimensional Gaussian fitting algorithm in ImageJ. Obtained traces were fit using a custom-written step-finding algorithm with a least-squares minimization[25]. All of the traces were visually checked for the goodness of the fit, and manual adjustments were implemented in less than 5% of the analysed steps.

Optical trapping assay. Sea urchin axonemes were immobilized on a glass coverslip in a flow chamber. The chamber was washed with 50 μl DLBC. Microtubule polarity of surface-immobilized axonemes was determined by adding ~2 nM TMR-labelled dynein into the chamber in DLBC with 10 μM ATP, waiting for 4 min to allow accumulation of TMR–dynein at the minus end of the microtubule and washing the chamber with 150 μl DLBC supplemented with 0.5 U ml^{-1} apyrase to consume the left-over ATP in the assay chamber[16]. TMR signals on axonemes were visualized with a CMOS camera (Hamamatsu) under 532 nm TIRF excitation. N-terminally GFP-tagged motors were mixed with GFP-antibody-coated polystyrene beads (0.86-μm diameter, Invitrogen)[19]. The motor–bead mixture was diluted tenfold in DLBC supplemented with the PCA/PCD oxygen scavenging system and 0.5 U ml^{-1} apyrase, and flown into the chamber. The motor:bead ratio was adjusted to a level at which 5–15% of the trapped beads that are brought near an axoneme bind to a microtubule within 1 min. Over 90% of the microtubule-binding events were terminated with a single release step, indicative of the binding of a single dynein monomer to a microtubule.

A force-feedback-controlled optical trap was custom built using a 2 W 1,064-nm continuous wave laser (Coherent), a Nikon Ti-Eclipse microscope body and a Nikon 100× 1.49 NA oil immersion objective. Typically, 0.86-μm diameter beads were trapped by a ~50-mW laser beam to obtain a spring constant of ~0.05 pN nm^{-1}. The trapping beam was steered by a two-axis acousto-optical deflector (AA Electronics) to trap freely diffusing monodispersed beads, lower them over surface-immobilized sea urchin axonemes and oscillate the bead ± 150 nm along the long axis of the microtubule at 1 Hz. Trap stiffness was calibrated for each sample by trapping a bead 3 μm above the surface of the coverslip, and fitting the power spectrum of a bead to a Lorentzian curve[30]. The bead displacement was detected by a position sensitive detector (PSD, First Sensor) located at a plane conjugate to the back focal plane of the objective. The PSD data were recorded at 20 kHz for calibration and 5 kHz for data acquisition. The PSD response was calibrated by acousto-optical deflector raster scanning of the laser beam across a trapped bead in both *x* and *y* directions, and a cubic polynomial fitting of the resulting curve. This calibration was repeated at the surface to avoid systematic errors in stiffness calibration. The data acquisition software monitored bead-trap separation in real time to prevent back-and-forth oscillations of the trap during a binding event. Microtubule release events were determined with a step-finding algorithm[31]. Dwell times were binned by applied force, and cumulative distribution function of each bin was fitted into a two-exponential decay function.

For force-feedback assays, beads were sparsely coated with full-length GFP–$Dyn_{RK+7hep}$ and brought into proximity with the axonemes. The trap was moved ± 500 nm along length of axonemes. When the bead-trap separation reached 100 nm after dynein binds to a microtubule, force-feedback control was activated and the trap position was updated at 100 Hz to keep the applied force constant. Trap stiffness was adjusted to exert constant forces between 0.75 and 3 pN. The velocity of the movement was calculated by the slope of the bead trajectories. Runs shorter than 0.6 s were excluded from data analysis.

ATPase assays. The microtubule-stimulated ATPase assays were performed using an EnzCheck Phosphate Assay Kit (Life Technologies) and a 96-well plate reader (μQuant, BioTek Instruments). A typical reaction has 2 nM dynein, 200 nM methylthioguanosine, 1 U ml^{-1} purine nucleoside phosphorylase, 2 mM DTT, 1 mM ATP, 0 or 50 mM KCl and varying concentrations of taxol-stabilized microtubules in DLB. Absorbances at 360 nm were measured with 60-s intervals for 30 min, blanked with buffer-only solution and calibrated against a P_i absorbance calibration curve. k_{basal} and k_{cat} were determined by fitting the data to the Michaelis–Menten equation in Origin.

Statistical analysis. χ^2 test was used to determine the *P* values for comparing the backward-stepping probability in stepping analysis. A two-sided *t*-test was used to determine the *P* values in the rest of the comparisons. All were calculated in MATLAB (Mathworks).

Atomic model building. The pre-power stroke conformation of human dynein-2 in the presence of Mg·ADP·Vi (PDB 4RH7[11]) was selected for the starting point of the Dyn molecular dynamics simulations. Mutations in the crystal structure were reversed (R1413K, Q2871R and V3680A) with the mutator plugin in VMD. An additional valine residue at the C terminus was removed. Missing residues (A2584–A2586, T2827–S2846, V3596–R3611 and D3954–S3963) were constructed using the Molefacture plugin of VMD and geometrically optimized via molecular dynamics simulations to fit the missing regions to obtain structurally complete Dyn. In brief, these residue stretches were modelled as unstructured conformations and flanked with the secondary structures of their neighbouring residues from the crystal structure. Each peptide was minimized for 10,000 steps, followed by 1 ns of equilibration simulations in a water box containing 150 mM KCl. After equilibration, 10-ns-long targeted molecular dynamics simulations[32] were performed for each peptide to position neighbouring residues towards their crystal coordinates. Subsequently, a final set of molecular dynamics simulations was performed by keeping the C_α atoms of neighbouring residues constrained at their crystal coordinates for 10 ns. Among these molecular dynamics trajectories, conformers that did not show a spatial overlap with the crystal structure were incorporated into the crystal structure. Dyn_{RK} was constructed with insertions of V2981P, P2983A, P3108A and E3110P mutations to the Dyn structure. $Dyn_{RK+7hep}$ was modelled by extending residues V2964–V2965 on coiled-coil 1 (CC1) and K3122–T3123 on coiled-coil 2 (CC2) using the conformation of residues R2916–V2964 on CC1 and T3123–A3171 on CC2.

Molecular dynamics simulations. Each dynein structure was solvated in a water box (using TIP3P water model) with a padding of at least 15 Å of water in each direction. Systems were ionized to 1 mM $MgCl_2$ and 150 mM KCl. Dyn, Dyn_{RK} and $Dyn_{RK+7hep}$ systems were composed of 781,332, 781,319 and 946,159 atoms, respectively. Molecular dynamics simulations were run in NAMD 2.11[33] using the CHARMM36 all-atom additive protein force field[34] with a time step of 2 fs. For van der Waals interactions, a 12 Å cut-off distance was used. The particle-mesh Ewald method was used to calculate long-range electrostatic interactions. The temperature was kept constant at 310 K using a damping coefficient of 1 ps^{-1} for Langevin dynamics. The pressure was maintained at 1 atm using the Langevin Nosé–Hoover method with an oscillation period of 100 fs and damping time scale of 50 fs. The protein was fixed for 10,000 steps of minimization followed by 2 ns of equilibration. Subsequently, constraints on the protein were released and the system was minimized for an additional 10,000 steps, followed by 6 ns of equilibration. Harmonic potential with a spring constant of 2 kcal mol^{-1} $Å^{-2}$ were applied to the backbone atoms during the first 2 ns of equilibration simulations.

All molecular dynamics simulations were performed at Istanbul Technical University (ITU) using NAMD with NVIDIA CUDA acceleration. Three separate simulations were performed for Dyn and Dyn_{RK} and one simulation was performed for $Dyn_{RK+7hep}$. The total simulation time was 1.7 μs. Starting conformations for three different Dyn_{RK} simulation (Dyn_{RK1}, Dyn_{RK2} and Dyn_{RK3}) were constructed based on the final conformations of three Dyn simulations (Dyn_1, Dyn_2 and Dyn_3). Similarly, $Dyn_{RK+7hep}$ was modelled on the basis of the final conformations obtained in Dyn_1 simulation. The conformations of Dyn_{+3hep} were estimated by elongating each molecular dynamics conformation of Dyn with the conformation of residues R2916–V2964 between V2964 and V2965 on CC1, and with residues T3123–A3171 between K3122 and T3123 on CC2. Dyn_{-3hep} conformations were estimated by shortening R2916–V2964 on CC1 and T3123–A3171 on CC2.

Stalk angle calculations. The dynein crystal structure (PDB 4RH7[11]) and each of the Dyn, Dyn_{RK} and $Dyn_{RK+7hep}$ conformations sampled during molecular dynamics simulations were docked onto tubulin by aligning with the C_α atoms of the microtubule–MTBD contact residues in the high-affinity *Mus musculus* dynein MTBD–tubulin complex (PDB 3J1T[22]), corresponding to residues L3300–D3307, A3313–I3325, E3333–R3341 and P3377–A3383 in 3J1T and E2998–S3005, D3011–L3023, W3031–A3039, P3076–A3082 in 4RH7. Principal axes (PA) of microtubules were obtained via the orient tool in VMD. PA1 (longitudinal axis) corresponds to the longitudinal axis of tubulin. PA2 (radial axis) passes through the centre of mass of the Q2982 and Q3098 C_α at the stalk–MTBD intersection of 4RH7 (Extended Data Fig. 3a). PA3 (tangential axis) is perpendicular to PA1 and PA2. The stalk vector (pointing from S3248 C_α to S3100 C_α) was projected on the plane constructed by PA1 and PA2. The angle between the projected vector and PA2 was defined as stalk angle.

LSV angle calculations. The post-power stroke conformation of the linker of *Dictyostelium discoideum* cytoplasmic dynein (PDB 3VKG[10]) was superimposed onto molecular dynamics conformers by aligning CC2 between the residues V3174–L3214 on both conformations. LSV was defined as the displacement vector between the C_α atoms of the N terminus residue V1258 of the pre-power stroke conformer and A1526 of the post-power stroke conformation. Dynein–tubulin complexes were superimposed onto the microtubule structure (PDB 5SYF[35]) by aligning C_α atoms of the tubulin α–1B chain. PA1 (longitudinal axis) of LSV corresponds to the longitudinal axis of the microtubule. PA2 (radial axis) is perpendicular to PA1 and passes through the C_α of V1258 of 4RH7. PA3 (tangential axis) is perpendicular to both PA1 and PA2. LSV was projected onto the plane defined by PA1 and PA3, and the angle that the projected vector makes with PA1 was defined as the LSV angle.

Reporting summary. Further information on research design is available in the Nature Research Reporting Summary linked to this paper.

Code availability. The custom analysis software for 3D tracking on this study is available online at https://github.com/YildizLab/RotationalAnalysisCode.git.

Data availability

The generated yeast strains and the data that support the findings of this study are available from the corresponding author upon request.

27. Chrétien, D., Kenney, J. M., Fuller, S. D. & Wade, R. H. Determination of microtubule polarity by cryo-electron microscopy. *Structure* **4**, 1031–1040 (1996).
28. Gell, C. et al. Purification of tubulin from porcine brain. *Methods Mol. Biol*. **777**, 15–28 (2011).
29. Yildiz, A. et al. Myosin V walks hand-over-hand: single fluorophore imaging with 1.5-nm localization. *Science* **300**, 2061–2065 (2003).
30. Neuman, K. C. & Block, S. M. Optical trapping. *Rev. Sci. Instrum*. **75**, 2787–2809 (2004).
31. Dogan, M. Y., Can, S., Cleary, F. B., Purde, V. & Yildiz, A. Kinesin's front head is gated by the backward orientation of its neck linker. *Cell Rep.* **10**, 1967–1973 (2015).
32. Schlitter, J., Engels, M. & Krüger, P. Targeted molecular dynamics: a new approach for searching pathways of conformational transitions. *J. Mol. Graph*. **12**, 84–89 (1994).
33. Phillips, J. C. et al. Scalable molecular dynamics with NAMD. *J. Comput. Chem*. **26**, 1781–1802 (2005).
34. Best, R. B. et al. Optimization of the additive CHARMM all-atom protein force field targeting improved sampling of the backbone φ, ψ and side-chain χ_1 and χ_2 dihedral angles. *J. Chem. Theory Comput*. **8**, 3257–3273 (2012).
35. Kellogg, E. H. et al. Insights into the distinct mechanisms of action of taxane and non-taxane microtubule stabilizers from cryo-EM structures. *J. Mol. Biol*. **429**, 633–646 (2017).
36. Alushin, G. M. et al. High-resolution microtubule structures reveal the structural transitions in $\alpha\beta$-tubulin upon GTP hydrolysis. *Cell* **157**, 1117–1129 (2014).

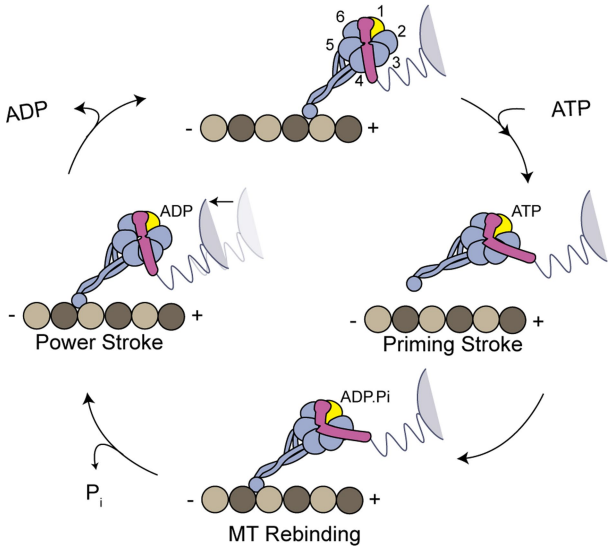

Extended Data Fig. 1 | Mechanochemical cycle of dynein. a, The AAA+ ring of a dynein monomer lies parallel to the microtubule, and the stalk is tilted towards the plus end at its base. In the absence of a nucleotide (apo) at AAA1, dynein is tightly bound to microtubules and the linker has a straight post-power stroke conformation, exiting the ring at AAA4. ATP binding to AAA1 (yellow) triggers microtubule release through a shift in the registry of a coiled-coil stalk, and the linker undergoes the priming stroke. At this pre-power stroke conformation, the linker is bent by a flexible hinge towards the middle of the ring and exits the ring at AAA2. The LSV is aligned with the long axis of the microtubule, and moves the MTBD towards the minus end. After ATP hydrolysis, the dynein head re-binds to the microtubule, and releases the inorganic phosphate (P_i). In the ADP-bound state, the linker undergoes a force-generating power stroke by moving back to its straight conformation. This pulls the cargo towards the minus end (black arrow). After ADP release, dynein returns back to the apo state for the next cycle.

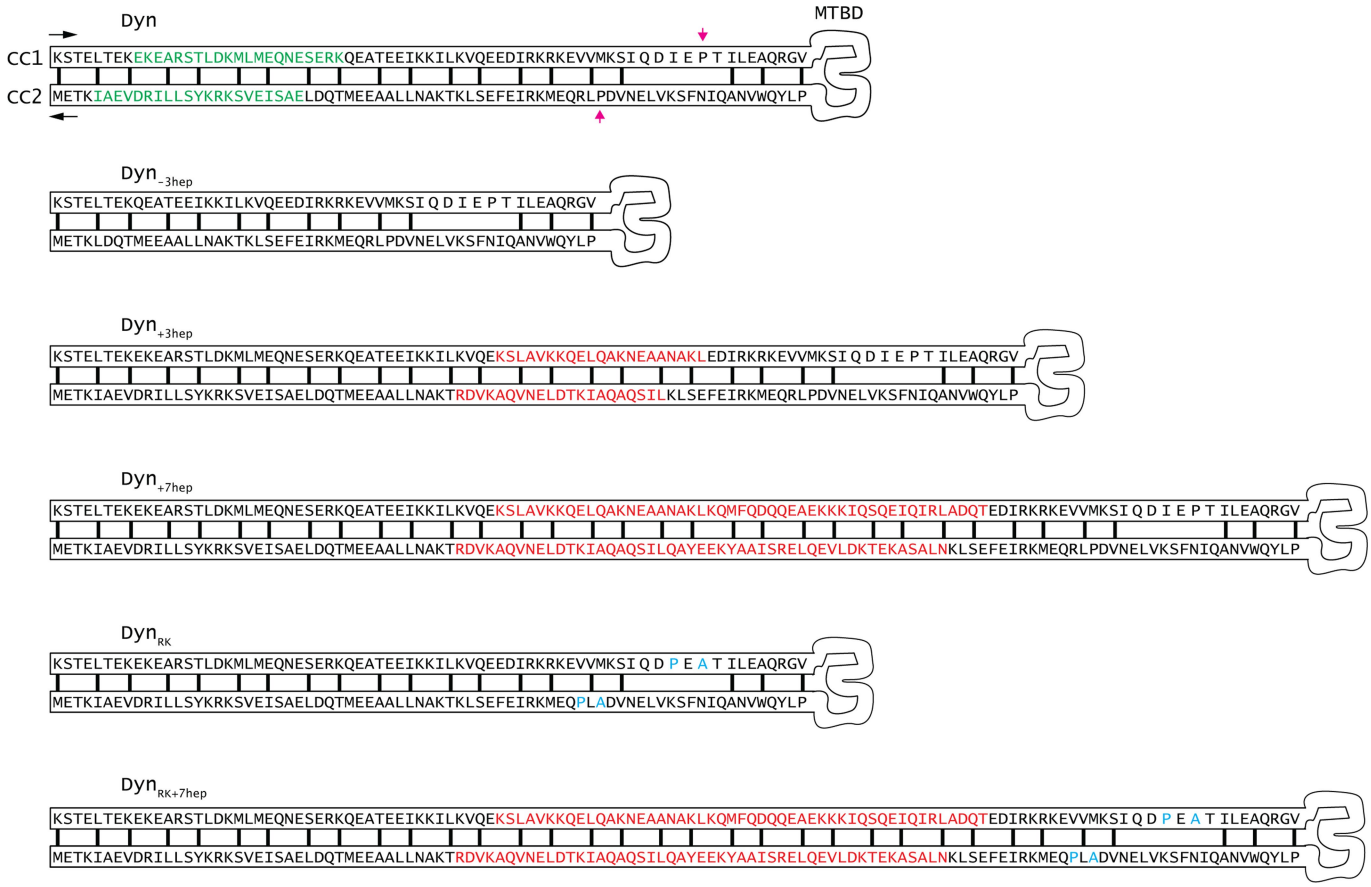

Extended Data Fig. 2 | Engineering the directionality of dynein motility. Schematic of the helices (CC1 and CC2) at the stalk of yeast cytoplasmic dynein shows the heptad repeat hydrophobic contacts (black lines) in the core of the coiled-coil, when dynein is in a low-microtubule-affinity (β) state. Conserved proline residues at the base of the Dyn stalk are highlighted by magenta arrows. The three heptads deleted from the stalk of Dyn_{-3hep} are highlighted in green in Dyn. The three- and seven heptad repeats inserted into Dyn_{+3hep}, Dyn_{+7hep} and $Dyn_{RK+7hep}$ are highlighted in red. The inserted sequences were taken from the *Drosophila melanogaster* cytoplasmic dynein[12]. Point mutations inserted into Dyn_{RK} and $Dyn_{RK+7hep}$ are highlighted in cyan.

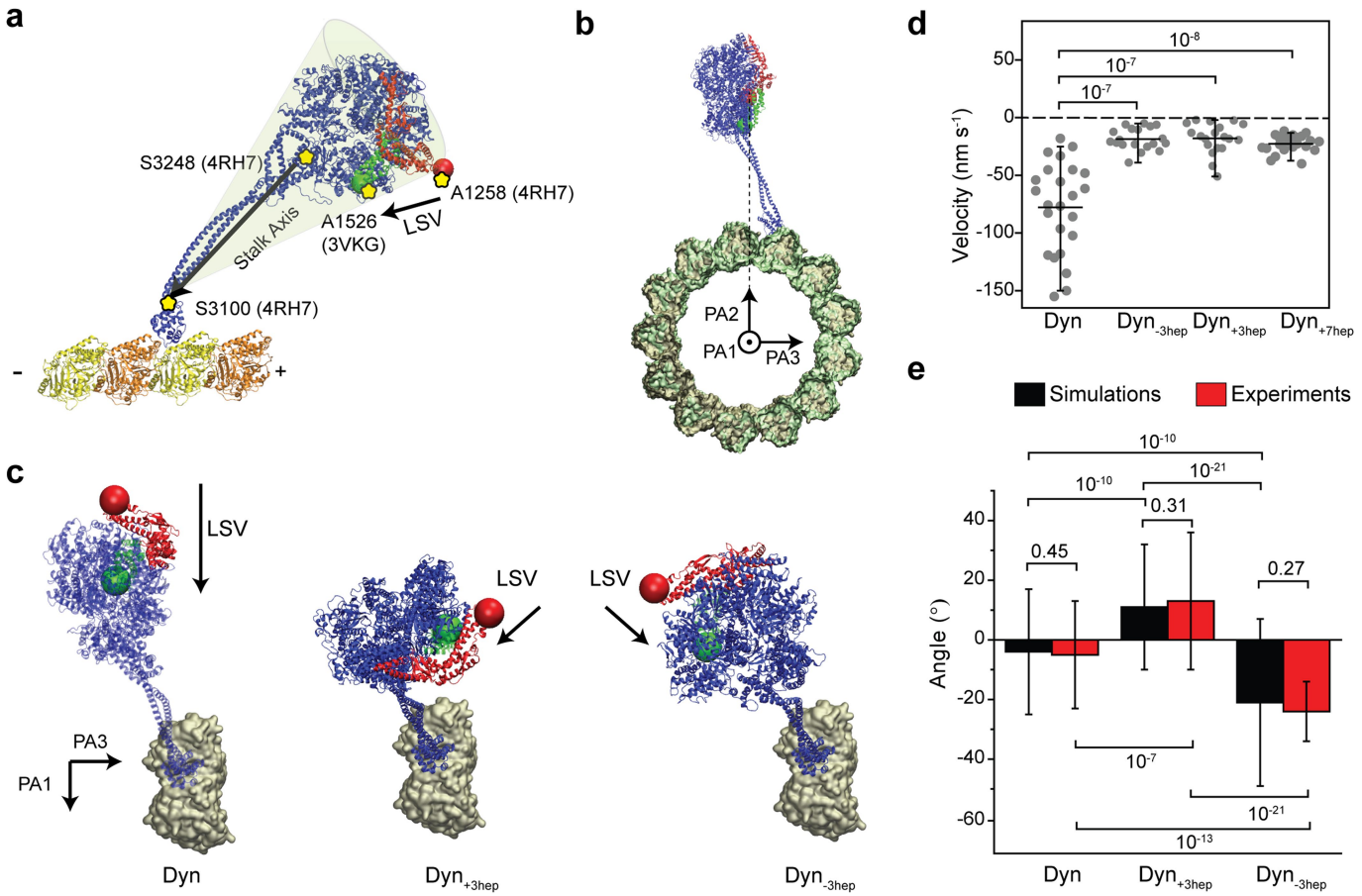

Extended Data Fig. 3 | Estimated orientation of the LSV relative to a microtubule as a function of stalk length. a, A Dyn monomer was manually docked onto a tubulin dimer (PDB 3VKG[10], 4RH7[11], 3J6G[36] and 5SYF[35]). The LSV was defined as the displacement vector of the N terminus of the linker from pre- (V1258 of PDB 4RH7, red bead) to post-power stroke (A1526 of PDB 3VKG, green bead) conformation. The stalk axis was defined as the vector that connects S3100 to S3248 (PDB 4RH7), which lies in the same plane with LSV of Dyn. **b**, Definition of the principal axes. Dyn was manually docked onto a microtubule. The longitudinal axis (PA1) is directed towards the minus end of the long axis of the microtubule. The radial axis (PA2) is directed from the microtubule centre-of-mass towards the pre-power stroke conformation of the linker (V1258 of PDB 4RH7, red bead). The tangential axis (PA3) is perpendicular to PA1 and PA2, as shown. **c**, The LSV (black arrow) of Dyn is aligned with the microtubule axis and is parallel to PA1. The expected orientations of Dyn_{+3hep} and Dyn_{-3hep} were modelled by alignment of the coiled-coils after insertions and deletions into the stalk. Insertion of three heptads into the stalk (Dyn_{+3hep}) is expected to reorient the ring and rotate the LSV_{short} clockwise with respect to the minus end of the microtubule. Shortening the stalk by three heptads (Dyn_{-3hep}) is expected to rotate the LSV_{short} anticlockwise. **d**, Velocity analysis of dynein-driven beads around microtubule bridges. All of the beads moved towards the minus end of the microtubule. $n = 24$, 20, 19 and 22 beads, from left to right. Centre line and error bars represent the mean and 5–95% confidence intervals. **e**, The comparison of the average LSV angles from molecular dynamics simulations ($n = 1{,}680$ conformations from 3 different simulations) and the average pitch angles from helical rotation of dynein-driven beads ($n_{beads} = 24$, 20 and 19, and $n_{rotations} = 99$, 59 and 72 for Dyn, Dyn_{+3hep}, and Dyn_{-3hep}, respectively) reveals that the LSV_{short} determines the helical directionality of dynein. Error bars represent s.d. In **d** and **e**, *P* values are calculated from a two-sided *t*-test.

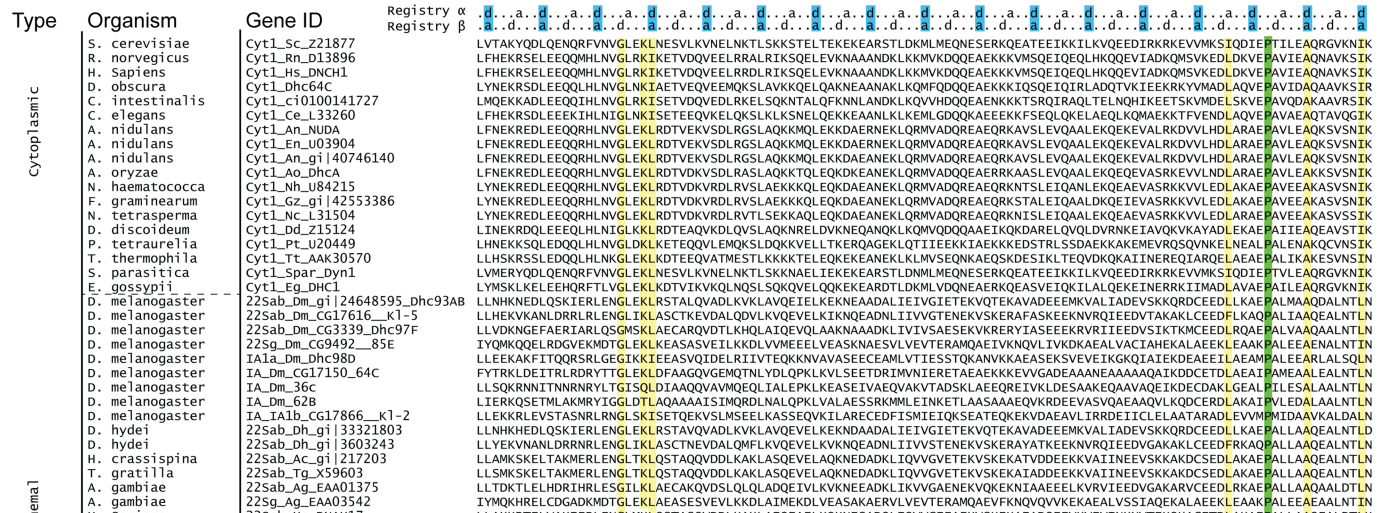

Extended Data Fig. 4 | Alignment of the CC1 of the stalk region in 67 dynein heavy chains. The sequences are oriented from the N terminus to the C terminus in these alignments. Isoforms of dynein used in the alignment were grouped on the basis of the type and the organism (cytoplasmic (cyt1), axonemal outer arm (22Sab, 22Sg), axonemal inner arm (IA) and intra-flagellar transport (cyt2) dyneins). The α and β registry of the stalk coiled-coils is shown on top. Stalk length is conserved among dyneins. Fully conserved proline residues at the base of the MTBD that cause tilting of the stalk coiled-coils towards the plus end of the microtubule are highlighted in green. Other residues that are conserved at over 90% are highlighted in yellow.

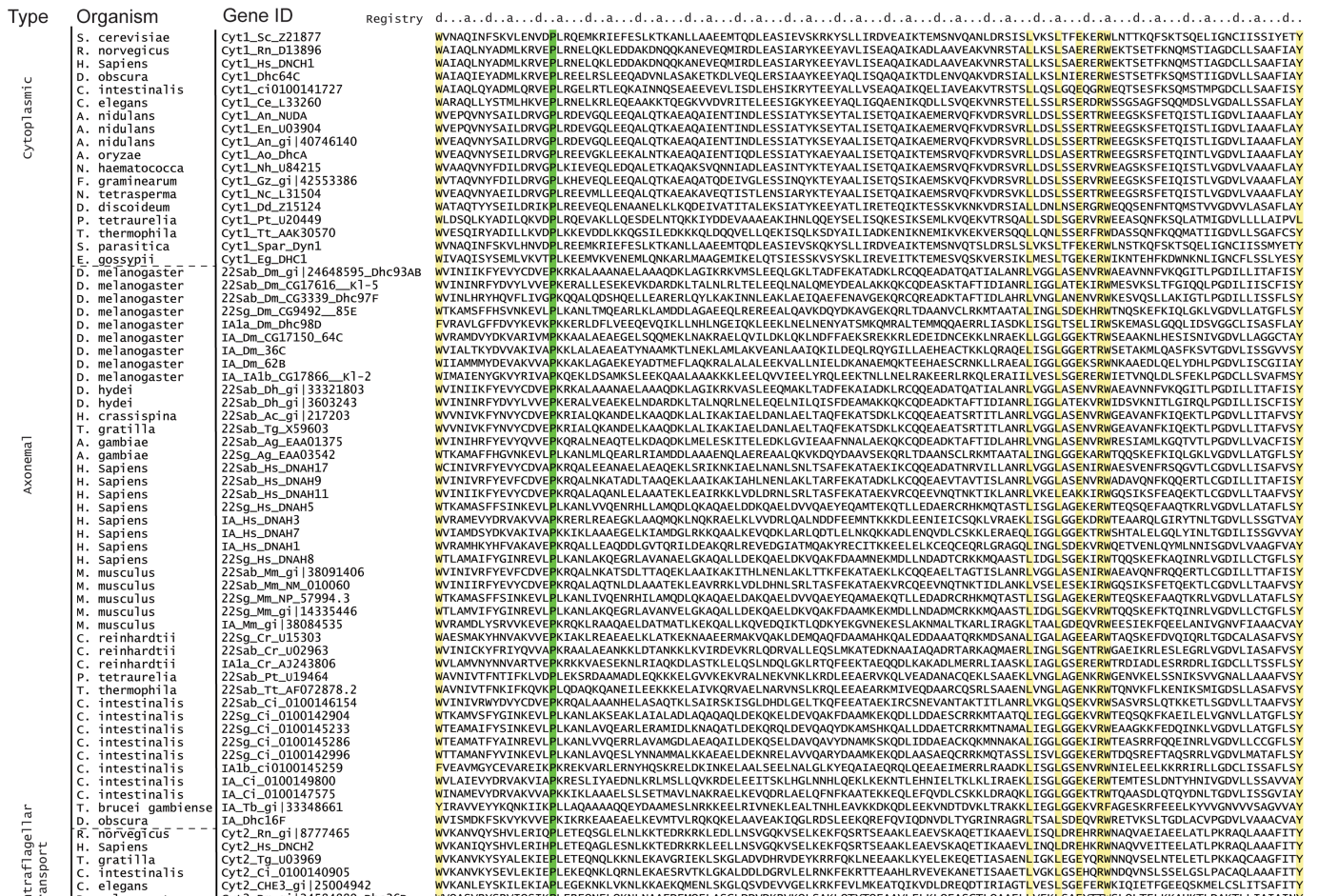

Extended Data Fig. 5 | Alignment of the CC2 of the stalk region in 67 dynein heavy-chains. The sequences are oriented from the N terminus to the C terminus in these alignments. Isoforms of dynein used in the alignment were grouped on the basis of the type and the organism (cytoplasmic (cyt1), axonemal outer arm (22Sab, 22Sg), axonemal inner arm (IA) and intra-flagellar transport (cyt2) dyneins). The α and β registry of the stalk coiled-coils is shown on top. Stalk length is conserved among dyneins. Fully conserved proline residues at the base of the MTBD that cause tilting of the stalk coiled-coils towards the plus end of the microtubule are highlighted in green. Other residues that are conserved at over 90% are highlighted in yellow.

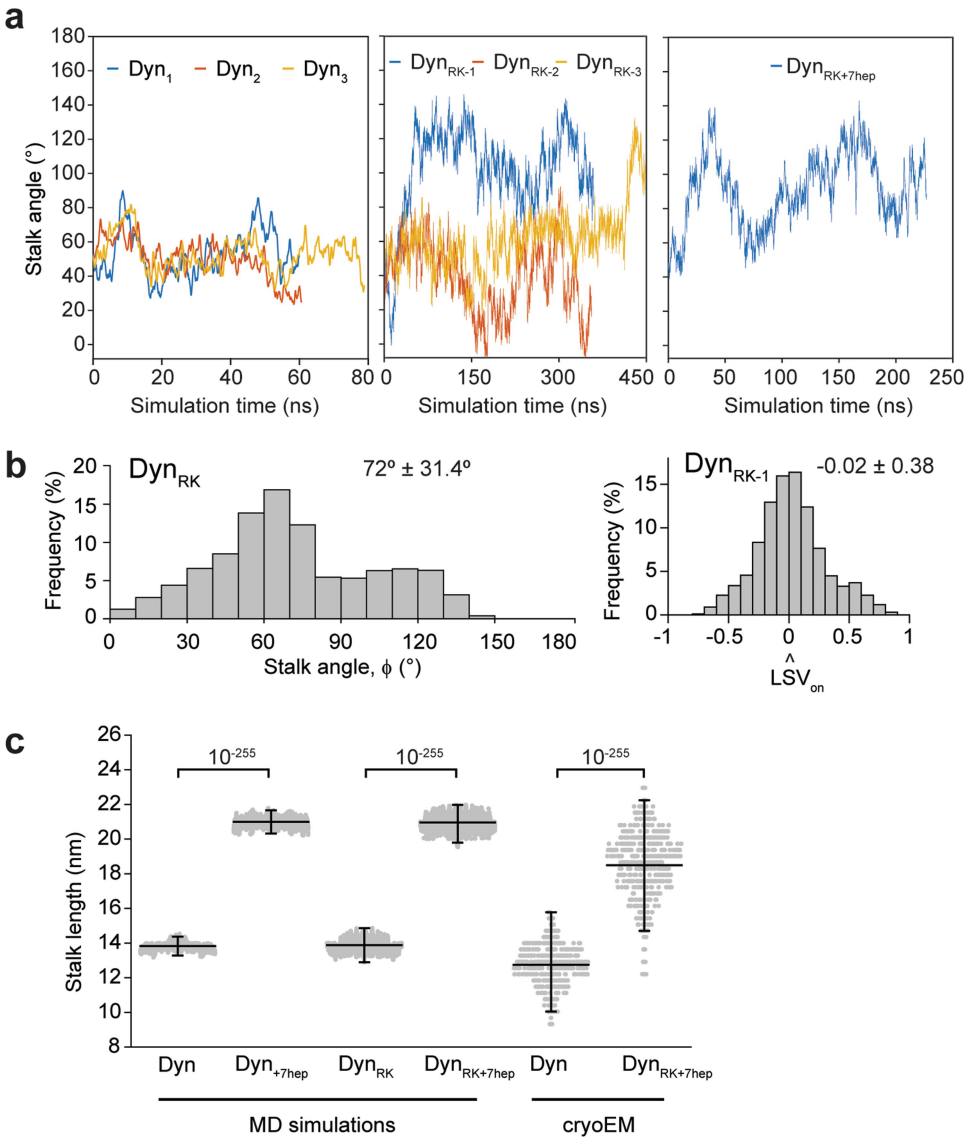

Extended Data Fig. 6 | Calculation of stalk and LSV angles by molecular dynamics simulations. a, Changes of the stalk angle in three independent molecular dynamics simulations of Dyn and Dyn_{RK}, and one simulation of $Dyn_{RK+7hep}$. In the Dyn_{RK1} and Dyn_{RK3} simulations, the stalk angle sharply increases around 50 ns and 400 ns, respectively and remains pointed towards the minus end after its reversal; 180° represents the tilting of the stalk towards the minus end. **b**, Left, stalk angle distribution for the Dyn_{RK} simulations; 180° represents the tilting of the stalk towards the minus end of the microtubule. Right, the length of the LSV unit vector projected onto the long axis of the microtubule after the reversal of the stalk in Dyn_{RK1}; −1 corresponds to LSV pointed towards the minus end. **c**, Stalk length distributions from molecular dynamics simulations and cryo-EM experiments (mean ± s.d., $n = 2{,}400$, 2,400, 7,263, 7,263, 392 and 421 conformations, from left to right). Centre line and error bars represents the mean and 5–95% confidence intervals. *P* values are calculated from a two-sided *t*-test.

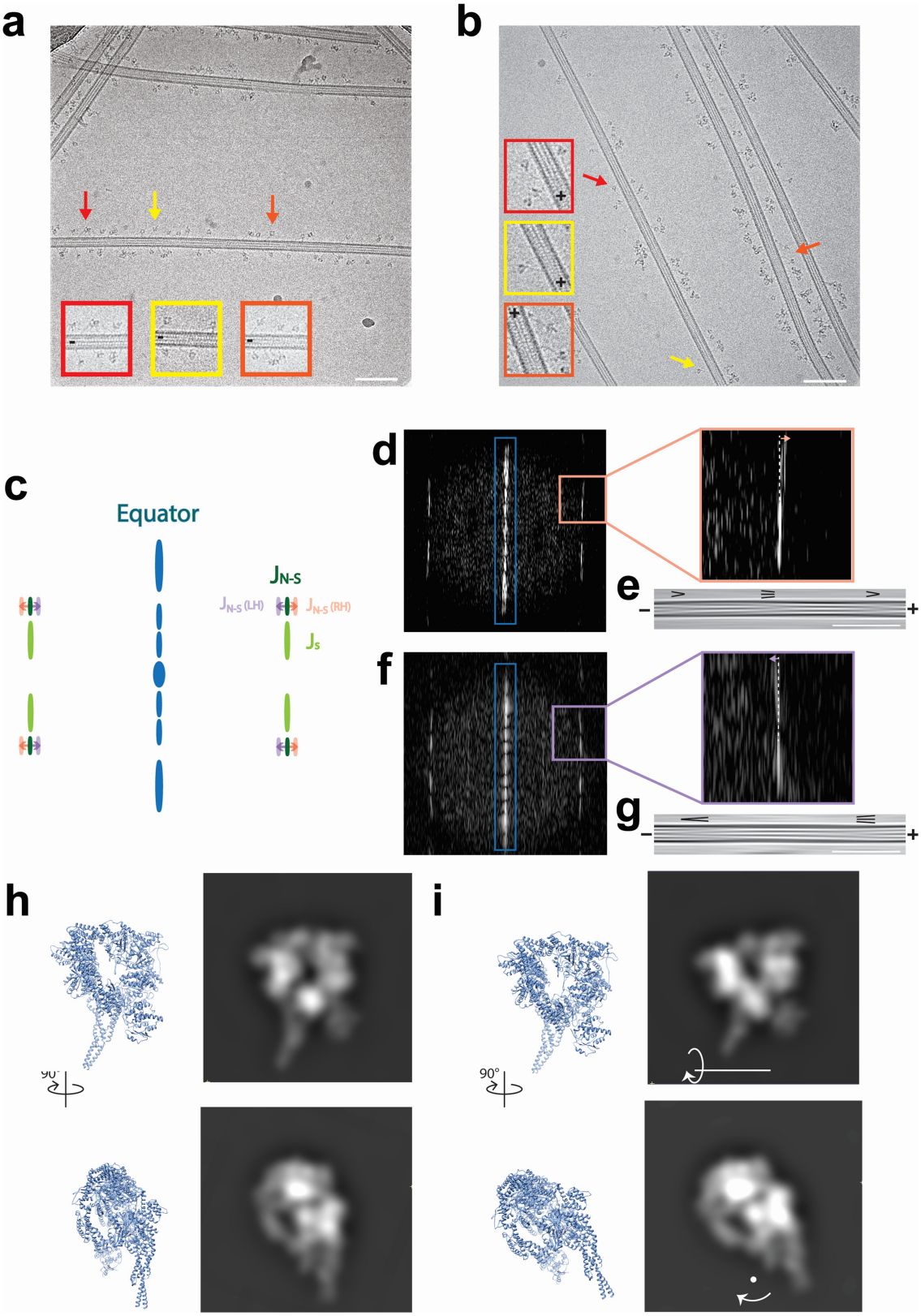

Extended Data Fig. 7 | See next page for caption.

Extended Data Fig. 7 | Cryo-EM image analysis of dynein monomers on microtubules. a, A representative cryo-electron micrograph of Dyn monomers bound to microtubules with single monomers indicated with arrows, and enlarged insets. Scale bar, 100 nm. $n = 98$ micrographs from 1 grid for Dyn, and 235 micrographs from 2 grids for $Dyn_{RK+7hep}$. **b**, A representative cryo-electron micrograph of $Dyn_{RK+7hep}$ monomers bound to microtubules with single monomers indicated with arrows, and enlarged insets. Scale bar, 100 nm. **c**, A simplified depiction of the power spectrum of a microtubule as a method to determine microtubule polarity. Microtubules with different numbers of protofilaments have different degrees of protofilament skew around the long axis. This causes differences in the Moiré patterns produced in cryo-EM images. These visual changes result in changes to the position of certain reflections in the microtubule power spectrum. As a result, right- and left-handed helix architectures can be differentiated by the relative positions of the J_S (light green) and J_{N-S} (dark green) reflections. For right-handed helices, the J_{N-S} (RH, pink) reflection is further from the equator (blue) than the J_S reflection, whereas for left-handed helices the J_{N-S} (LH, purple) reflection is closer to the equator than the J_S reflection. When the microtubule is Fourier-filtered to only include information from the equator (blue), a characteristic arrowhead pattern is formed from the Moiré patterns. For right-handed helix architectures, this points towards the plus end; for left-handed helix architectures, this points towards the minus end. Thirteen protofilament microtubules were not included in the analysis because they have no protofilament skew. **d**, An example power spectrum of an microtubule determined to be a right-handed helix. The enlargement on the right shows that the J_S reflection is closer to the equator than the J_{N-S} reflection. **e**, A Fourier-filtered image produced from the equatorial reflections from the power spectrum in **d** (blue box). For right-handed helix architectures, the arrowheads point towards the plus end. Scale bar, 100 nm. **f**, An example power spectrum of an microtubule determined to be a left-handed helix. The enlargement on the right shows that the J_S reflection is further from the equator than the J_{N-S} reflection. **g**, A Fourier-filtered image produced from the equatorial reflections from the power spectrum in **f** (blue box). For left-handed helix architectures, the arrowheads point towards the minus end. Scale bar, 100 nm. **h**, Orthogonal views of an atomic model of a dynein motor in an arrangement corresponding to the wild-type view, and synthetic projections produced from them. In this arrangement, the motor appears as an even ring. **i**, As in **h**, but with the model tilted 30° around the indicated axis. In this arrangement, the projection creates a crescent shape similar to that seen in the $Dyn_{RK+7hep}$ class (Fig. 2e), albeit with the ring and stalk unflipped; this suggests that the ring of $Dyn_{RK+7hep}$ is slightly tilted in relation to the microtubule.

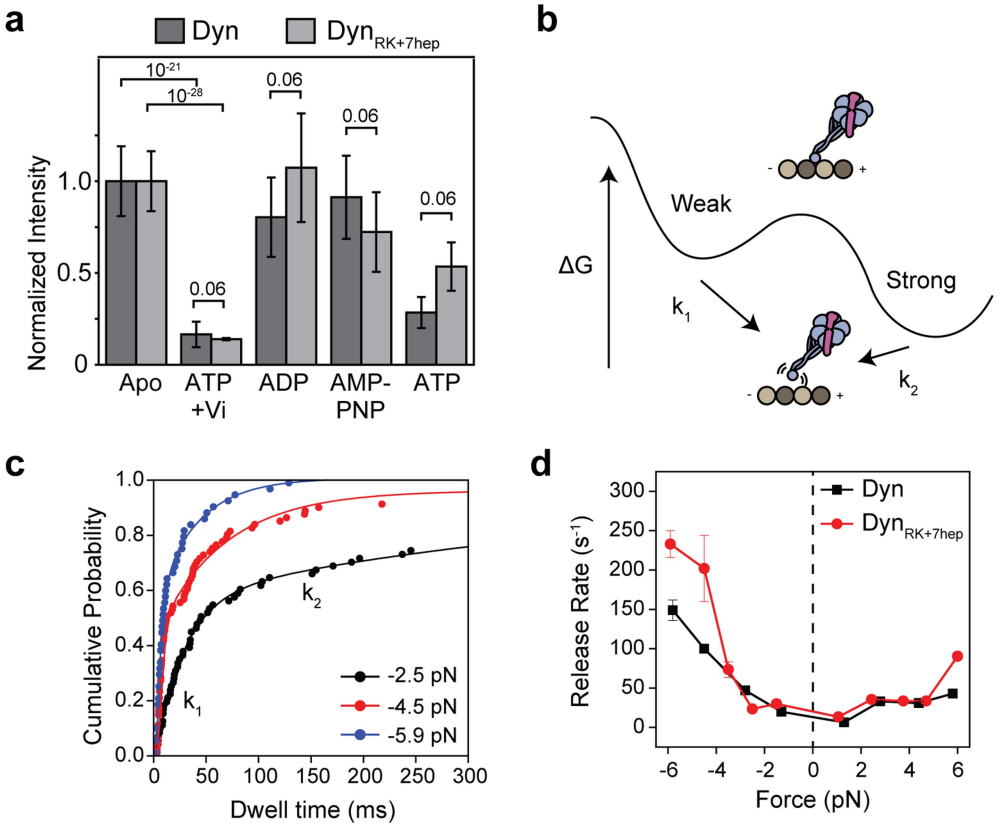

Extended Data Fig. 8 | Nucleotide- and force-induced release of Dyn and Dyn$_{RK+7hep}$ monomers from microtubules. a, The normalized intensity of 100 nM GFP-tagged Dyn and Dyn$_{RK+7hep}$ monomers on sea urchin axonemes under given nucleotide conditions. Similar to Dyn, Dyn$_{RK+7hep}$ released from microtubules in the ADP–P_i state, mimicked by ATP and vanadate (Vi, $n = 40$ axonemes from three independent measurements, mean ± s.d.). *P* values are calculated from a two-sided *t*-test. **b**, A model of the dynein–microtubule interaction shows two distinct binding modes in the apo state, with k_1 and k_2 representing force-induced release rates from the weak and strong states, respectively. The slow rate (k_2) represents strong binding of the motor to its tubulin binding site, whereas the fast rate (k_1) represents transient or nonspecific interactions of the motor with the microtubule. **c**, Cumulative probability distributions (solid circles) of the microtubule-bound time of Dyn monomers at given force ranges. The release rates (k_1 and k_2) were calculated by a two-exponential-decay fit (solid curves). **d**, Calculated k_1 values from the exponential fit (± 95% confidence intervals) to the Dyn$_{RK+7hep}$ dwell time has similar force-dependence to Dyn. Each bin contains 120 dwells from 2 independent measurements.

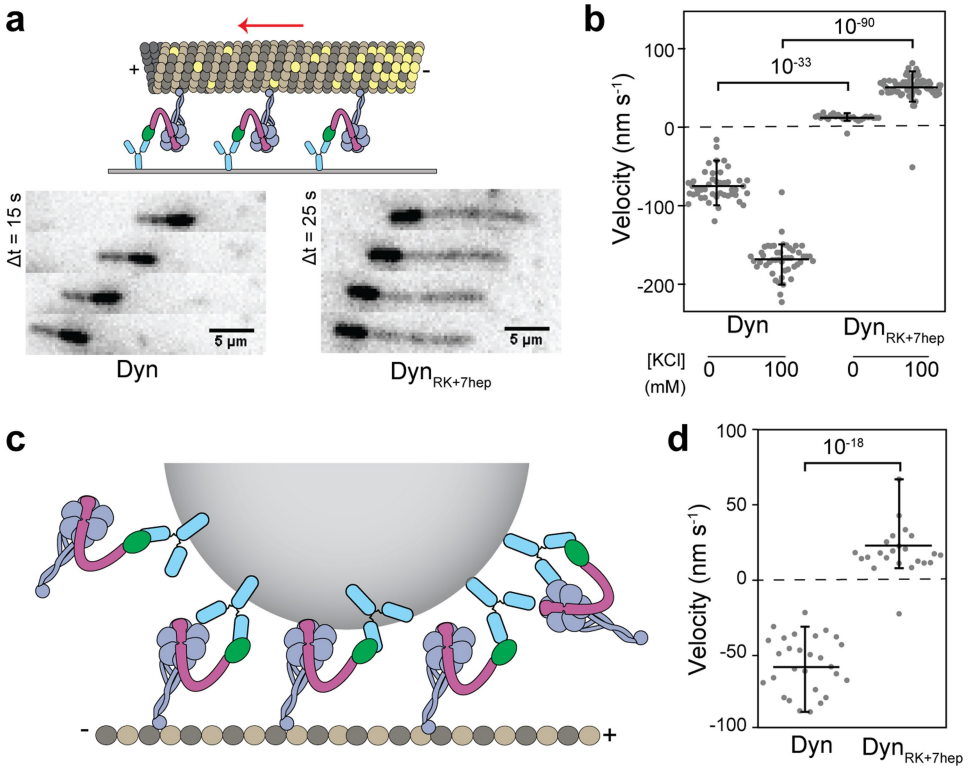

Extended Data Fig. 9 | Dyn$_{RK+7hep}$ monomers exhibit robust plus-end directionality in microtubule gliding and bead-motility assays. a, Top, schematic of the microtubule gliding assay with monomeric dynein. Bottom, images from time-lapse recordings show gliding of polarity-marked microtubules by Dyn and Dyn$_{RK+7hep}$ monomers. Dyn glides microtubules with their plus end ahead, whereas Dyn$_{RK+7hep}$ glides microtubules towards the opposite direction. $n = 3$ biological replicates. **b**, Microtubule gliding velocity and directionality of Dyn and Dyn$_{RK+7hep}$ in the presence and absence of 100 mM KCl. Negative velocities correspond to minus-end directionality. $n = 45$, 47, 27 and 70 from left to right, from two independent measurements. **c**, Schematic of the bead-motility assay with monomeric dynein (not to scale). N-terminally GFP-tagged monomers are attached to 860-nm diameter GFP-antibody-coated beads from their tail. **d**, Velocities of the beads driven by Dyn and Dyn$_{RK+7hep}$ monomers. $n = 29$ and 24 from left to right, from three independent experiments. In **b** and **d**, the centre line and edges represent the mean and 5–95% confidence intervals, respectively. *P* values are calculated from a two-sided *t*-test.

Extended Data Table 1 | Engineering and testing of dynein mutants

a

	Dyn - 0 mM KAc	Dyn - 50 mM KAc	$Dyn_{RK+7hep}$ - 50 mM KAc	$Dyn_{RK+7hep}$ - 150 mM KAc
k_{cat} (s^{-1} per head)	7.3 ± 0.1	7.9 ± 0.1	6.8 ± 0.2	8.5 ± 0.2
k_{basal} (s^{-1} per head)	1.1 ± 0.1	2.4 ± 0.1	4.6 ± 0.6	6.6 ± 0.3
K_M (nM)	19 ± 3.4	630 ± 65	19 ± 5.1	75 ± 4.3
+ Runs (nm s^{-1})	N.A.	N.A.	18.2 ± 10.9	23.9 ± 13.8
- Runs (nm s^{-1})	88.2 ± 30.2	95.5 ± 51.5	10.6 ± 3.6	33.3 ± 11.1
+ Runs (%)	0	0	81	83
- Runs (%)	100	100	8	6
Diffusive (%)	0	0	10	11

b

Strain ID	Construct Name	Description	Source	Dataset
VY208	GFP-GST-Dyn-DHA	GFP-3xHA-GST-331DYN1-gs-DHA	ref. 4	F1c,d, F4c,d, EDF3d
VY268	DHA-GST-Dyn	DHA-GST-331DYN1	ref. 4	F3c F4c,e, EDT1a
VY209	FRB-Dyn-DHA	3xHA-FRB-331DYN1-gs-DHA	ref. 4	F2e,f, EDF6c, EDF7
Y144	GFP-Dyn-FKBP-DHA	GFP-3xHA-331DYN1-gsgsgsgs-FKBP12 URA3	ref.16	F3a,b,e, EDF9
Y124	GFP-Dyn_{-3hep}-DHA	GFP-3xHA-331DYN1-(-$3hep_{3036/3292}$)-331DYN1-gs-DHA	This study	F1c,d, EDF3d
Y200	GFP-GST-Dyn_{+3hep}-DHA	GFP-3xHA-GST-331DYN1-(+$3hep_{3085/3159}$)-331DYN1-gs-DHA	This study	F1c,d, EDF3d
Y123	GFP-Dyn_{+7hep}-DHA	GFP-3xHA-331DYN1-(+$7hep_{3085/3159}$)-331DYN1-gs-DHA	ref. 12	F4b, EDF3d
Y197	GFP-GST-Dyn_{RK}-DHA	GFP-3xHA-GST-$331DYN1_{I3101P/P3103A-P3229A/R3231P}$	This study	F4b
Y187	GFP-GST-$Dyn_{RK+7hep}$-DHA	GFP-3xHA-GST-$331DYN1_{I3101P/P3103A}$-(+$7hep_{3085/3159}$)-$331DYN1_{P3229A/R3231P}$-gs-DHA	This study	F3c, F4a,b,c,e
Y198	GFP-$Dyn_{RK+7hep}$-DHA	GFP-HA-$331DYN1_{I3101P/P3103A}$-(+$7hep_{3085/3159}$)-$331DYN1_{P3229A/R3231P}$-gs-DHA	This study	F3a,b,e, EDF8, EDF9
Y201	FRB-$Dyn_{RK+7hep}$-DHA	3xHA-FRB-$331DYN1_{I3101P/P3103A}$-(+$7hep_{3085/3159}$)-$331DYN1_{P3229A/R3231P}$-gs-DHA	This study	F2e,f, EDF6c, EDF7
Y202	GFP-471$Dyn_{RK+7hep}$-DHA	GFP-3xHA-471$DYN1_{I3101P/P3103A}$-(+$7hep_{3085/3159}$)-$331DYN1_{P3229A/R3231P}$-gs-DHA	This study	F4d, EDT1a

a, Microtubule-stimulated ATPase activity and velocity analysis of Dyn and $Dyn_{RK+7hep}$ under different salt conditions. An increase in salt concentration reduces the Michaelis–Menten constant (K_M) of Dyn and $Dyn_{RK+7hep}$ for microtubules, but it does not alter their directionality. K_M of Dyn without added salt is similar to that of $Dyn_{RK+7hep}$ under 50 mM KAc (two-sided *t*-test, $P = 0.055$). ATPase data were collected from three independent experiments (mean ± s.d.). $n = 67, 55, 52$ and 58, from left to right.

b, The list of yeast strains used in this study. These strains were produced by homologous recombination using the template strain (MATa his3-11,5 ura3-1 leu2-3, 112 ade2-1 trp-1 pep4::HIS3 prb1Δ) expressing the tail-truncated yeast cytoplasmic dynein (331Dyn1) under the galactose promoter (pGal) or full-length dynein (471DYN1) under the native promoter. A ZZ–Tev tag was inserted at the N termini of these constructs for affinity purification. The DHA tag was used to label the motor with fluorescent dyes functionalized with alkyl chloride. F, Figure; EDF, Extended Data Figure; EDT, Extended Data Table.

nature research

Corresponding author(s): Ahmet Yildiz

Last updated by author(s): Dec 19, 2018

Reporting Summary

Nature Research wishes to improve the reproducibility of the work that we publish. This form provides structure for consistency and transparency in reporting. For further information on Nature Research policies, see Authors & Referees and the Editorial Policy Checklist.

Statistics

For all statistical analyses, confirm that the following items are present in the figure legend, table legend, main text, or Methods section.

n/a	Confirmed	
☐	☒	The exact sample size (*n*) for each experimental group/condition, given as a discrete number and unit of measurement
☐	☒	A statement on whether measurements were taken from distinct samples or whether the same sample was measured repeatedly
☐	☒	The statistical test(s) used AND whether they are one- or two-sided *Only common tests should be described solely by name; describe more complex techniques in the Methods section.*
☐	☒	A description of all covariates tested
☐	☒	A description of any assumptions or corrections, such as tests of normality and adjustment for multiple comparisons
☐	☒	A full description of the statistical parameters including central tendency (e.g. means) or other basic estimates (e.g. regression coefficient) AND variation (e.g. standard deviation) or associated estimates of uncertainty (e.g. confidence intervals)
☐	☒	For null hypothesis testing, the test statistic (e.g. *F*, *t*, *r*) with confidence intervals, effect sizes, degrees of freedom and *P* value noted *Give P values as exact values whenever suitable.*
☒	☐	For Bayesian analysis, information on the choice of priors and Markov chain Monte Carlo settings
☒	☐	For hierarchical and complex designs, identification of the appropriate level for tests and full reporting of outcomes
☒	☐	Estimates of effect sizes (e.g. Cohen's *d*, Pearson's *r*), indicating how they were calculated

Our web collection on statistics for biologists contains articles on many of the points above.

Software and code

Policy information about availability of computer code

Data collection	For hardware control of microscope: Labview 2017 For image acquisition: Andor Solis For Nikon Microscope Body Control: Ti Control 4.4.2
Data analysis	For CTF determination: GCTFv1.08 For classification: Relion 2.1 For image handling: FIJI 1.0 For volume filtering: Bsoft 1.6.0 For molecular dynamics simulations and plotting: NAMD, VMD For data analysis: MATLAB (R2017), Imagej (v.1.51r), Origin Pro 9.0

For manuscripts utilizing custom algorithms or software that are central to the research but not yet described in published literature, software must be made available to editors/reviewers. We strongly encourage code deposition in a community repository (e.g. GitHub). See the Nature Research guidelines for submitting code & software for further information.

Data

Policy information about availability of data

All manuscripts must include a data availability statement. This statement should provide the following information, where applicable:

- Accession codes, unique identifiers, or web links for publicly available datasets
- A list of figures that have associated raw data
- A description of any restrictions on data availability

The generated yeast strains, coding and the data that support the findings of this study are available from the corresponding author upon request.

Field-specific reporting

Please select the one below that is the best fit for your research. If you are not sure, read the appropriate sections before making your selection.

☒ Life sciences ☐ Behavioural & social sciences ☐ Ecological, evolutionary & environmental sciences

For a reference copy of the document with all sections, see nature.com/documents/nr-reporting-summary-flat.pdf

Life sciences study design

All studies must disclose on these points even when the disclosure is negative.

Sample size	No pre-determined sample size was used in the experimental design. No fewer than 40 motors, 25 microtubules and 15 beads were used to make a conclusion. The sample size chosen is in line with previous studies in the field. For electron microscopy, the sample size represents the total number of particles picked from the micrographs collected.
Data exclusions	For EM classes, data that was not computationally assigned to the given class was excluded. This eliminates the user-based variability in data analysis. For dynein single motility assays, diffusive molecules and molecules with short run lengths (<2pixel or <200 nm) were excluded from velocity and directionality analysis due to diffraction-limit of conventional light microscopy. In microtubule gliding assays, MTs without a clear ploarity (i.e. double bright end, no clear bright end) were excluded from the analysissince directionality cannot be determined. In optical trap assays, attachments that are shorter than 2.5ms were excluded due to the time resolution limit of the microscope (1 ms).
Replication	Microscopy and biochemical assays were reproduced from 3 independent datasets collected from samples prepared with different protein purifications. For cryoelectron microscopy, Dyn data was collected from one grid in one session, DynRK+7hep data was collected over two sessions, from two grids made on different days. Molecular dynamics results were obtained from 3 independent simulations. Optical trap data were reproduced from 2 independent experiments.
Randomization	For EM analysis, data from the two groups (Dyn and DynRK+7hep) were processed independently from each other.
Blinding	Blinding was not performed for EM and single molecule data since the appearance of the micrographs (specifically, the microtubule and particle density) and kymographs could be placed into two groups without prior knowledge.

Reporting for specific materials, systems and methods

We require information from authors about some types of materials, experimental systems and methods used in many studies. Here, indicate whether each material, system or method listed is relevant to your study. If you are not sure if a list item applies to your research, read the appropriate section before selecting a response.

Materials & experimental systems

n/a	Involved in the study
☐	☒ Antibodies
☐	☒ Eukaryotic cell lines
☒	☐ Palaeontology
☒	☐ Animals and other organisms
☒	☐ Human research participants
☒	☐ Clinical data

Methods

n/a	Involved in the study
☒	☐ ChIP-seq
☒	☐ Flow cytometry
☒	☐ MRI-based neuroimaging

Antibodies

Antibodies used	Custom made anti-GFP antibodies (Covance Inc. - Custom Antisera, Animal No: CA5315) were purified by GFP affinity chromatography and diluted to 0.4 mg/ml for microtubule gliding assays and coating of carboxylated latex beads.
Validation	N/A

Eukaryotic cell lines

Policy information about cell lines

Cell line source(s)	Template S. cerevisiae strains were received from the laboratory of Ronald D. Vale. New strains are generated from these strains using homologous recombination.
Authentication	Cells were not authenticated.
Mycoplasma contamination	Cells were not checked for mycoplasma contamination.
Commonly misidentified lines (See ICLAC register)	not applicable